The lncRNA Malat1 Inhibits miR-15/16 to Enhance Cytotoxic T Cell Activation and Memory Cell Formation

Benjamin D Wheeler[1,2], John D Gagnon[1,2], Wandi S Zhu[1,2], Priscila Muñoz-Sandoval[1,2], Simon K Wong[1], Dimitre R Simeonov[1], Zhongmei Li[3], Rachel Debarge[1,3,4], Matthew H Spitzer[1,3,4,5,6], Alexander Marson[1,3,7], K Mark Ansel[1,2]

1: Department of Microbiology & Immunology, University of California San Francisco, San Francisco, CA 94143, USA
2: Sandler Asthma Basic Research Program, University of California, San Francisco, San Francisco, CA, USA
3: Gladstone-UCSF Institute of Genomic Immunology, San Francisco, CA 94158, USA
4: Department of Otolaryngology-Head and Neck Surgery, University of California San Francisco, San Francisco, CA 94143, USA
5: Parker Institute for Cancer Immunotherapy, San Francisco, CA 94129
6: Chan Zuckerberg Biohub, San Francisco, CA 94158
7: Department of Medicine, University of California San Francisco, San Francisco, CA 94143, USA

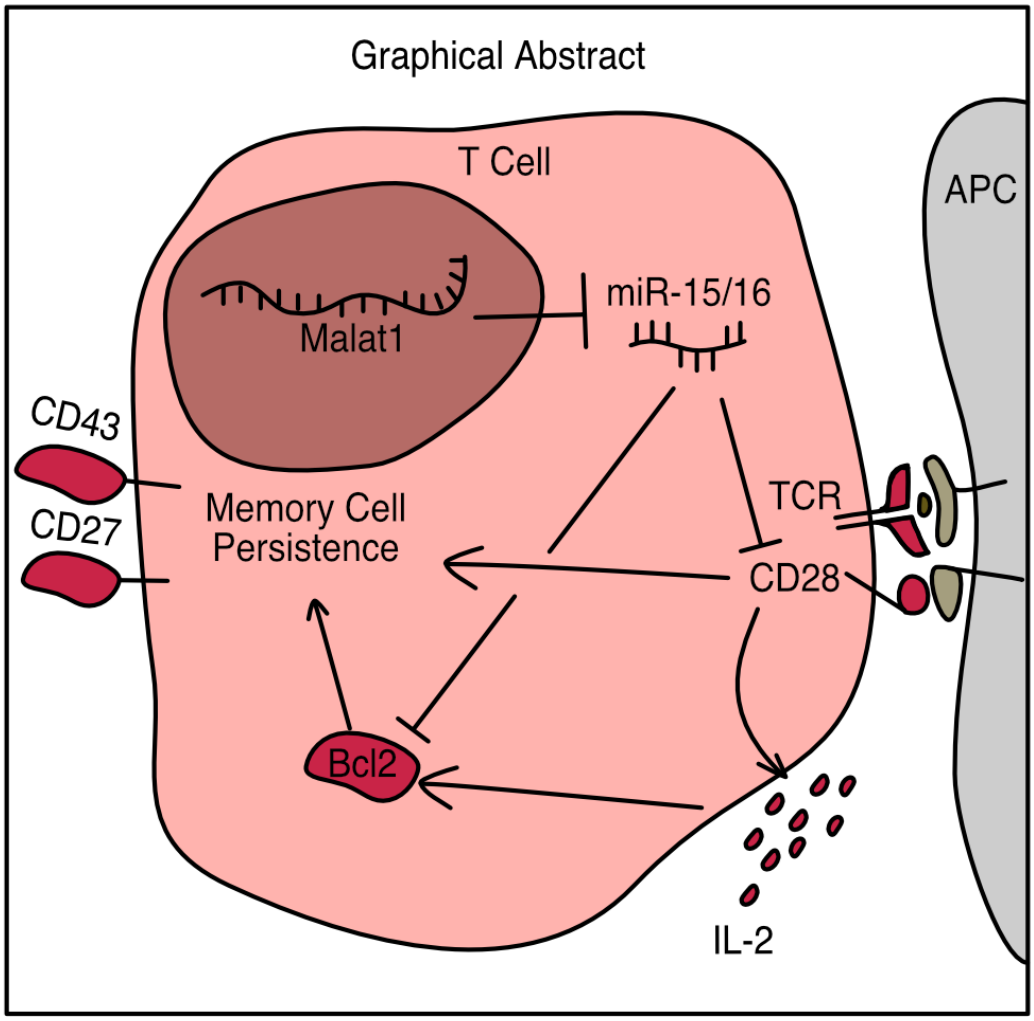

Abstract

Proper activation of cytotoxic T cells via the T cell receptor and the costimulatory receptor CD28 is essential for adaptive immunity against viruses, many intracellular bacteria and cancers. Through biochemical analysis of RNA:protein interactions, we uncovered a non-coding RNA circuit regulating activation and differentiation of cytotoxic T cells composed of the long non-coding RNA Malat1 (Metastasis Associated Lung Adenocarcinoma Transcript 1) and the microRNA family miR-15/16. miR-15/16 is a widely and highly expressed tumor suppressor miRNA family important for cell proliferation and survival. miR-15/16 also play important roles in T cell responses to viral infection, including the regulation of antigen-specific T cell expansion and T cell memory. Comparative Argonaute-2 high throughput sequencing of crosslinking immunoprecipitation (Ago2 HITS-CLIP, or AHC) combined with gene expression profiling in normal and miR-15/16-deficient T cells revealed a large network of several hundred direct miR-15/16 target mRNAs, many with functional relevance for T cell activation, survival and memory formation. Among these targets, the long non-coding RNA Malat1 contained the largest absolute magnitude miR-15/16-dependent AHC peak in T cells. This binding site was also among the strongest lncRNA:miRNA interactions detected in the T cell transcriptome. We used CRISPR targeting with homology directed repair to generate mice with a 5-nucleotide mutation in the miR-15/16 binding site in Malat1. This mutation interrupted Malat1:miR-15/16 interaction, and enhanced the repression of other miR-15/16 target genes, including CD28. Interrupting Malat1 interaction with miR-15/16 decreased cytotoxic T cell activation, including the expression of IL-2 and a broader CD28-responsive gene program. Accordingly, Malat1 mutation diminished memory cell persistence following LCMV Armstrong and *Listeria monocytogenes* infection. This study marks a significant advance in the study of long noncoding RNAs in the immune system by ascribing cell-intrinsic, sequence-specific *in vivo* function to Malat1. These findings have implications for T cell-mediated autoimmune diseases, antiviral and anti-tumor immunity, as well as lung adenocarcinoma and other malignancies where Malat1 is overexpressed.

Introduction

Cytotoxic T cells are indispensable for mounting an adaptive immune response against intracellular pathogens and the clearance of mutated cells such as cancer. Over the course of a viral infection, cytotoxic T cells are primed by antigen presenting cells and undergo extensive rounds of intense proliferation (Murali-Krishna et al., 1998). As they clonally expand, these cells differentiate into effector and memory cells and acquire effector functions, including the production of cytotoxins and critical cytokines such as IL-2, TNFα, and IFNγ (Bachmann et al., 1999). As the infection is cleared, the cytotoxic T cell response contracts as many cells die via apoptosis, yielding a long lived pool of memory cells poised for secondary expansion and protection against reinfection with the same pathogen (Badovinac et al., 2002; Wherry and Ahmed, 2004). The factors that control this expansion, differentiation, and contraction have been intensely researched in the past decades, focusing in large part on proteins such as transcription factors, signaling enzymes, and cytokines (Chen et al., 2018). However, it is of recent interest to understand how non-protein coding regions of the genome contribute to the regulation of these cells as well. These non-protein coding elements can be regulatory in nature such as enhancers (Roychoudhuri et al., 2016; Shapiro et al., 1997-7), or RNA species that are transcribed but not translated. Two such species of interest to our present study are microRNAs (miRNAs) and long non-coding RNAs (lncRNAs).

MicroRNAs are short (21 nucleotide) RNAs which, when loaded into Argonaute (Ago) proteins, can target mRNAs that contain complementary seed sequences in their 3' UTRs for translation inhibition and degradation(Bartel, 2018; Djuranovic et al., 2012; Eichhorn et al., 2014). In particular, the miR-15/16 family are

potent regulators of cell cycle and survival (Liu et al., 2008). Previous work from our group utilized conditional deletion of the four major miR-15/16 family members (miR-15a, miR-15b, miR-16-1, miR-16-2) driven by CD4-cre transgene (hereafter referred to as miR-15/16$^{\Delta/\Delta}$ mice or T cells) to demonstrate that this miRNA family has important effects on cytotoxic T cells (Gagnon et al., 2019). In response to viral infection, miR-15/16$^{\Delta/\Delta}$ mice generate more viral-antigen specific T cells, and these cells preferentially differentiate into memory cells that express CD127 and CD27 (Gagnon et al., 2019).

In contrast to the well defined roles of miRNAs, lncRNAs as a class do not have a single defined function. They are broadly defined as RNAs transcribed by polymerase II, over 200 nucleotides (nt) in length, that lack a translated open reading frame (Su et al., 2021; Wilusz et al., 2009). Some lncRNAs bind to chromatin and regulate nearby or distant genes, and others scaffold transcription factors and other protein complexes (Kopp and Mendell, 2018). Most relevant to the present study, some lncRNAs act as competing endogenous RNAs (ceRNAs) that bind to miRNAs, preventing their binding to and subsequent repression of mRNA targets (Poliseno et al., 2010; Su et al., 2021). However, rigorous connections between lncRNA physiological functions and molecular mechanisms of action has been hampered by the lack of precise tools to facilitate their study (Ponting and Haerty, 2022). As lncRNAs lack an open reading frame, insertion or deletion (indel) mutations do not reliably create null alleles. Instead, investigators have frequently deleted large genomic regions around the promoter or excised the genomic locus of the transcript altogether. These approaches risk disrupting cis-regulatory elements or topologically associated domains that control other nearby genes. Other studies that identified physiological roles for lncRNAs rely on RNAi-mediated lncRNA degradation. Both this approach and genetic manipulations that block lncRNA transcription leave a mechanistic gap between sequence features and downstream function. Studies demonstrating sequence dependent function of lncRNAs are comparatively rare (Carrieri et al., 2012; Elguindy and Mendell, 2021; Faghihi et al., 2008; Gong and Maquat, 2011; Kleaveland et al., 2018; Lee et al., 1999; Yoon et al., 2012).

One lncRNA that has garnered much attention is the Metastasis Associated Lung Adenocarcinoma Transcript 1 (Malat1). Malat1 was first identified as highly expressed in both malignant tumors and healthy lung and pancreas with high interspecies conservation (Ji et al., 2003). Malat1 is mostly localized to the nucleus, where it is found within nuclear speckles, although it is not necessary for their formation (Nakagawa et al., 2012). These characteristics have generated numerous hypotheses about the function of Malat1 including that it scaffolds epigenetic and splicing factors and acts as a ceRNA to inhibit a variety of miRNAs (Su et al., 2021; Tripathi et al., 2010).

In the immune system, Malat1 has been studied in dendritic cells, macrophages, T helper cells, T regulatory cells, and cytotoxic T cells (Hewitson et al., 2020; Kanbar et al., 2022; Masoumi et al., 2019; Wu et al., 2018). Malat1 is actively regulated during cytotoxic T cell differentiation with higher expression in memory precursors and lower expression in short-lived effector cells during LCMV infection (Kakaradov et al., 2017). Similarly, T cells stimulated *in vitro* express decreased levels of Malat1 over time (Masoumi et al., 2019). Early reports using large genetic deletions in the mouse Malat1 locus detected widespread gene expression changes but failed to identify a role for Malat1 in mouse development or cytotoxic T cell responses (Nakagawa et al., 2012; Yao et al., 2018; Zhang et al., 2012), though a recent report using RNAi detected altered T cell responses(Kanbar et al., 2022). Clearly there remains much to learn about the sequence-specific mechanisms by which Malat1 tunes pathways and functions essential to cytotoxic T cells.

In the present study, we present a non-coding RNA circuit that regulates the activating signals from CD28 and IL-2, leading to low Bcl-2 expression and loss of memory cells following LCMV infection. We do so by identifying candidate interactions between miRNAs and lncRNAs via a targeted biochemical approach, and by creating CRISPR-targeted transgenic mice with precise mutation of Malat1 to interrogate the physiological function of the interaction between miR-15/16 and Malat1. We use this novel mouse to identify CD28 responsive gene programs affected by this circuit, and provide a new sequence-specific function of Malat1 *in vivo*.

Results

Malat1 is highly Bound by miR-15/16

To identify candidate noncoding ceRNAs in cytotoxic T cells, we performed Argonaute-2 high throughput sequencing of crosslinking immunoprecipitation (Ago2 HITS-CLIP, AHC). Integrating sequence reads across different classes of transcribed genomic annotations revealed that lncRNAs are bound extensively by Ago2, but the median lncRNA had 7.8 times fewer aligned AHC sequence reads compared to 3' untranslated regions (UTRs) where miRNAs canonically bind to mRNAs (Fig. 1A). This difference likely reflects the comparatively low expression of many lncRNAs, and it highlights the relatively low occupancy of Ago2 on most of these transcripts. Nevertheless, there were individual lncRNAs that stood out as highly bound across the transcript. To prioritize lncRNAs for further investigation, we manually curated the transcripts with the largest number of aligned AHC sequence reads. Among the top 10 most highly bound transcripts, 3 overlapped with protein coding genes, 2 were on the mitochondrial chromosome, and 3 were repetitive annotations. Strikingly, all of the top 10 transcripts were either annotated as rRNA or contained an rRNA repeat element, except the 8th most bound transcript, Malat1 (Table 1). When the same analysis was repeated with rRNA repeats masked, Malat1 was the second most highly bound transcript (Table 2).

Table 1. lncRNAs with the most AHC reads

Noncode Gene ID	Total Reads	Chromosome	Alias	Note
NONMMUG018330.3	4766634	17	ENSMUST00000198477.1	Contains rRNA repeat
NONMMUG044354.2	2291785	M	mt-Rnr2	Overlaps mt-ND1
NONMMUG044353.2	1208170	M	mt-Rnr1	
NONMMUG076321.1	1012732	6		Overlaps and best aligns to NONMMUG034479.2
NONMMUG034478.3	1012015	6		Overlaps and best aligns to NONMMUG034479.2
NONMMUG034479.2	1011610	6		Contains rRNA repeat
NONMMUG007938.3	785970	11		Intronic of Gm36876, contains rRNA repeat(Weirick et al., 2016)
NONMMUG020671.2	383447	19	Malat1	
NONMMUG015781.2	336664	16		Intronic of Zc3h7a, contains rRNA repeat
NONMMUG044321.2	317822	9		Contained in Lars2 3’ UTR, contains rRNA repeat

Table 2. lncRNAs with the most AHC reads that do not align to rRNA repeat elements

Noncode Gene ID	Total Reads	Chromosome	Alias	Note
NONMMUG018330.3	688875	17	ENSMUST00000198477.1	Partially anti-sense to XR_877120.2, binding extends beyond rRNA repeat
NONMMUG020671.2	383447	19	Malat1	
NONMMUG094408.1	296723	6		Contains B4A/B3 SINE, binding restricted to SINE
NONMMUG005751.2	291393	11		Intronic of Dock2, contains multiple RLTR44-int repeat elements, binding restricted to RLTRs
NONMMUG094727.1	289326	6		Contains B4A/B3 SINE, binding is restricted to repeats
NONMMUG014644.3	241005	15	Pvt1	Many repeats, but binding is not restricted to any definite subset
NONMMUG096664.1	229834	15	PVt1	Splice variant of NONMMUG014644.3
NONMMUG024327.3	222686	2	Oip5os1, Cyrano	Well described in (Han et al., 2020)
NONMMUG026716.2	207631	3		Overlapping Mbnl1
NONMMUG094659.1	196269	6		Overlapping Foxp1

Malat1 has been proposed to inhibit miRNAs as a ceRNA (Chen et al., 12 2017; Luan et al., 2016; Qiao et al., n.d.; Wang et al., 2019; Wu et al., 2018; Xiao et al., 2015; Xie et al., 2017). We used the Piranha peak calling algorithm to identify sites with the highest degree of miRNA binding, as indicated by AHC sequence read number and density (Fig. 1B). Within cytotoxic T cells, the algorithm identified 55 AHC peaks in Malat1, the largest of which was extremely pronounced (Fig. 1C). Compared with other lncRNA binding peaks, this peak had the 36th most total aligned reads and the 142nd highest read density (15th and 16th respectively when rRNA reads are masked). Even when compared to peaks in 3' UTRs of mRNAs, the largest peak in Malat1 was the 100th most (98th percentile) bound peak in terms of read density (Fig. 1B).

miRTarget, the custom miRNA binding prediction algorithm (Liu and Wang, 2019), identified an 8-mer seed binding sequence of the miR-15/16 family centered within the most densely bound region of the called peak (Fig. 1C). miR-15/16 has not been previously shown to interact with Malat1 in mice, so to determine whether this peak is miR-15/16 dependent, we performed AHC with cultured $CD8^+$ miR-$15/16^{\Delta/\Delta}$ T cells. In the absence of miR-15/16, Ago2 binding to Malat1 was preserved throughout the whole transcript except for the peak containing the predicted miR-15/16 8-mer seed binding sequence (Fig. 1C). We conclude that miRNAs of the miR-15/16 family bind abundantly to Malat1. Further, miR-15/16 binding occurred in a region of high evolutionary conservation (Fig. 1D). The corresponding region containing the miR-15/16 binding site in human MALAT1 was highly enriched in two publicly available AHC datasets obtained using the 293 human embryonic kidney (HEK) cell line, consistent with Malat1 regulating miR-15/16 in a colorectal cancer cell line (Karginov and Hannon 2013; Ji et al. 2019; Li et al. 2018)(Fig. 1E). We conclude that miR-15/16 bind abundantly to Malat1 in mouse and human cells.

We hypothesized that Malat1 may inhibit the function of miR-15/16 in cytotoxic T cells. To directly address this question in mice, we used CRISPR-Cas9 with homology directed repair to generate mice in which five nucleotides of the miR-15/16 seed binding sequence within Malat1 were scrambled (Fig. 1F). Mice homozygous for this mutation are subsequently referred to as *Malat1*$^{scr/scr}$. To confirm the targeted functional outcome of this mutation, AHC was performed on cultured $CD8^+$ T cells isolated from *Malat1*$^{scr/scr}$ mice. Ago2 binding was preserved across the Malat1 transcript except at the mutated miR-15/16 binding site, where AHC sequence read density was greatly reduced (Fig. 1C). This finding confirmed that miR-15/16 binds to Malat1 at this site in a sequence dependent manner, and provided us with a tool for highly specific investigation of the functional consequences of Malat1:miR-15/16 interaction.

Figure 1. Malat1 is highly bound by miR-15/16

CD8+ T cells were isolated from spleens, grown *in vitro* for 5 days, then Ago2 transcriptomic occupancy was assayed via Ago2 HITS-CLIP.

(A-B) Transcriptome wide analysis of Ago2 HITS-CLIP libraries prepared from WT cells (combined libraries n =2).

(A) Summed reads across entire annotations. Line indicates total reads across the Malat1 transcript. Malat1 was #8 most highly bound lncRNA annotation, which was in the top 0.0091% of all lncRNA annotations analyzed with >0 HITS-CLIP reads.

(B) Ago2 HITS-CLIP peaks were identified and reads were summed within those called peaks that intersected with the given annotation. Peaks were of variable length so summed reads were normalized by peak length. Line indicates HITS-CLIP reads per nucleotide in the called peak containing the miR-15/16 binding site in Malat1. This peak was the #121 most bound HITS-CLIP peak in lncRNA peaks analyzed, which was in the top 2.3% of all evaluated peaks in lncRNAs.

(C) Ago2 HITS-CLIP binding to the mouse Malat1 locus reads from combined libraries shown (n = 2 for each genotype). Grey bar indicates the peak containing the miR-15/16 binding site. Black bars indicate regions identified as peaks by piranha. Blue bars indicate predicted binding sites of miRNAs expressed in our data set from the miRTarget custom sequence prediction algorithm. Grey bar indicates miR-15/16 binding peak.

(D) Local alignment of the human and mouse Malat1 sequences near the miR-15/16 conserved binding site. Highlighting indicates the depth of evolutionary conservation of k-mers as predicted by the lncLOOM algorithm (Ross et al., 2021).

(E)Ago2 HITS-CLIP binding to the human MALAT1 locus from publicly available data sets (Karginov and Hannon, 2013; Li et al., 2018). Blue vertical bar indicates the conserved miR-15/16 binding site.

(F) Schematic representing the creation of the *Malat1*^{scr} allele. Bases in red indicate the 5 nucleotides whose sequence was scrambled by CRISPR-Cas9 HDR to prevent miR-15/16 binding.

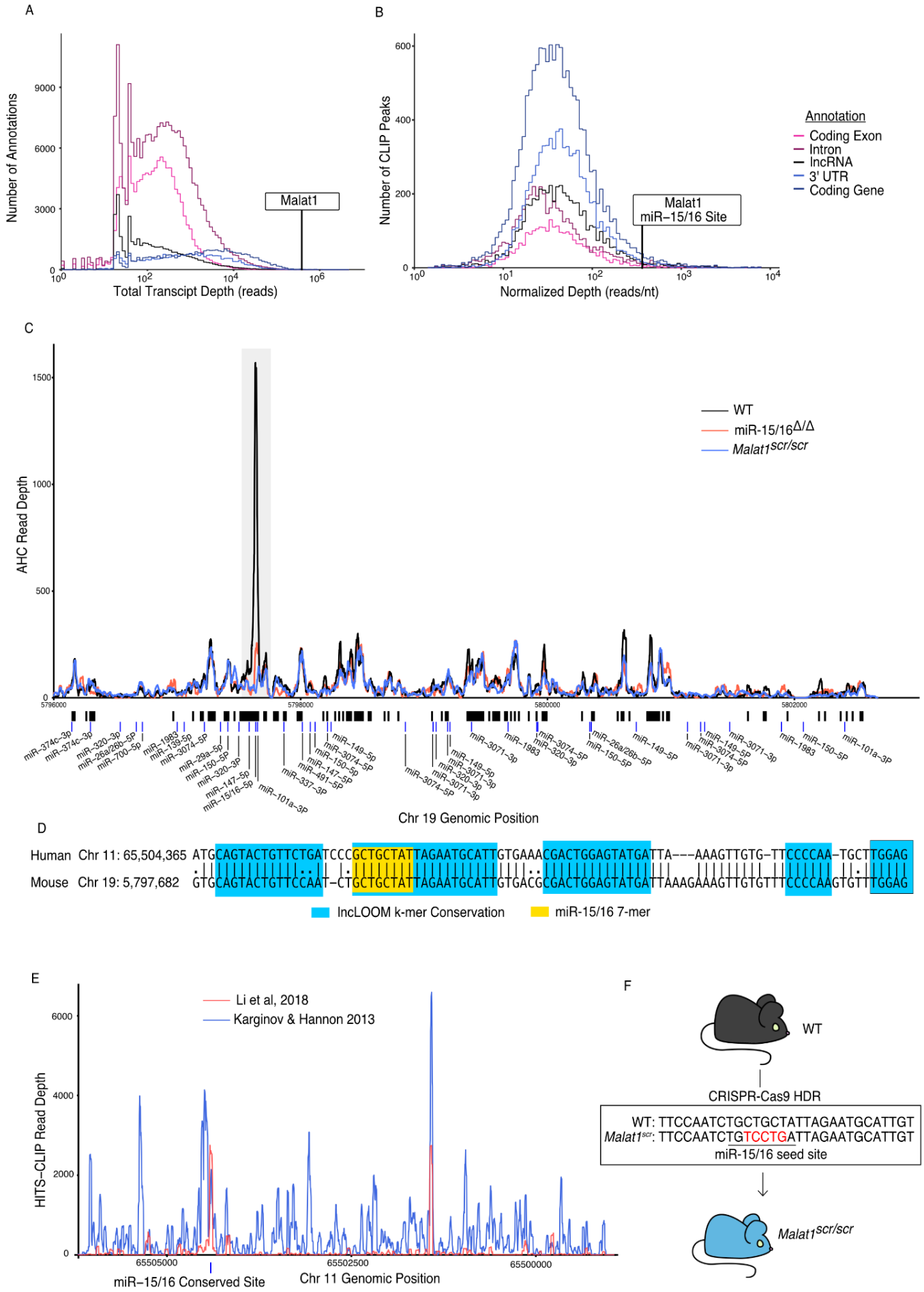
A
Number of Annotations
Total Transcipt Depth (reads)
Malat1
B
Number of CLIP Peaks
Normalized Depth (reads/nt)
Malat1
miR−15/16 Site
Annotation
Coding Exon
Intron
lncRNA
3' UTR
Coding Gene
C
AHC Read Depth
WT
miR-15/16Δ/Δ
Malat1scr/scr
Chr 19 Genomic Position
D
Human Chr 11: 65,504,365 ATGCAGTACTGTTCTGATCCCGCTGCTATTAGAATGCATTGTGAAACGACTGGAGTATGATTA---AAAGTTGTG-TTCCCCAA-TGCTTGGAG
Mouse Chr 19: 5,797,682 GTGCAGTACTGTTCCAAT-CTGCTGCTATTAGAATGCATTGTGACGCGACTGGAGTATGATTAAAGAAAGTTGTGTTTCCCCAAGTGTTTGGAG
lncLOOM k-mer Conservation
miR-15/16 7-mer
E
Li et al, 2018
Karginov & Hannon 2013
HITS−CLIP Read Depth
miR−15/16 Conserved Site
Chr 11 Genomic Position
F
WT
CRISPR-Cas9 HDR
WT: TTCCAATCTGCTGCTATTAGAATGCATTGT
Malat1scr: TTCCAATCTGTCCTGATTAGAATGCATTGT
miR-15/16 seed site
Malat1scr/scr

Malat1 inhibits miR-15/16 availability and activity

Malat1:miR-15/16 interaction could lead to regulation and/or degradation of the lncRNA, the miRNAs, or both. To assess whether miR-15/16 degrades Malat1 we compared the expression of Malat1 by mRNA sequencing in primary mouse $CD8^+$ T cells. Malat1 expression was unchanged in miR-15/16$^{\Delta/\Delta}$ cells as well as in the *Malat1*$^{scr/scr}$ cells (Fig. 2A). Previous studies investigating Malat1 and other lncRNAs as ceRNA inhibitors of miRNAs have suggested that inhibition occurs by either target RNA–directed miRNA degradation (TDMD) or stoichiometric sequestration of the miRNA from protein-coding mRNA targets (Han et al., 2020; Su et al., 2021). Therefore, we also tested the possibility that Malat1 lowers miR-15/16 abundance by TDMD or a related mechanism. However, in freshly isolated mouse $CD8^+$ T cells, miR-15b and miR-16 were unchanged and only miR-15a, a family member with lower expression, was modestly decreased in *Malat1*$^{scr/scr}$ cells (Fig. 2B). We conclude that Malat1 and the miR-15/16 family do not influence each other's absolute abundance in this setting.

To test whether Malat1 affects miR-15/16 function, we examined miR-15/16 target binding in our AHC data. We first defined an experimentally supported list of TargetScan predicted miR-15/16 binding sites with at least 1 AHC read in both WT and *Malat1*$^{scr/scr}$ cells. Using this list, we then examined the read depth at these sites in both *Malat1*$^{scr/scr}$ and WT cells (603 sites contained in 479 genes). In WT cells, these sites constituted on average 3.2% of the binding in each 3' UTR, and this figure increased to 3.4% in *Malat1*$^{scr/scr}$ cells, indicating that Ago2 occupancy preferentially increased at these sites when miR-15/16 binding to Malat1 was eliminated (Fig. 2C). To confirm that binding to these target sites was miR-15/16 dependent, we assessed their AHC read depths in miR-15/16$^{\Delta/\Delta}$ cells as well. As predicted, binding was greatly reduced in miR-15/16$^{\Delta/\Delta}$ cells, representing, on average, 1.0% of binding to a given 3' UTR, a 69% reduction in Ago2 binding compared to WT (Fig 2D). In contrast, no significant differences were observed for binding at predicted sites for the highly expressed miRNA families of miR-101, Let-7, miR-21, and miR-142, (Fig. S1). Thus, we conclude that the *Malat1*^{scr} allele specifically negatively regulates the first requirement of miR-15/16 function – binding to mRNA targets.

We next sought to investigate whether this increased binding resulted in decreased target mRNA expression. To do so, we analyzed mRNA-sequencing data from primary CD8+ T cells 24 hours after stimulation. We generated empirical CDF plots from these data comparing target gene expression in miR-15/16$^{fl/fl}$ to miR-15/16$^{\Delta/\Delta}$ cells as well as WT to *Malat1*$^{scr/scr}$ cells. For each of these comparisons, we then compared the distribution for miR-15/16 target genes, as defined above, to the distribution for all other expressed genes. In the case of WT to *Malat1*$^{scr/scr}$ cells, the distribution was shifted in favor of decreased target gene expression in the *Malat1*$^{scr/scr}$ cells (Fig 2E). In the case of miR-15/16$^{fl/fl}$ to miR-15/16$^{\Delta/\Delta}$, the distribution was shifted in favor of increased target gene expression in the miR-15/16$^{\Delta/\Delta}$ cells, indicating that this gene set is relieved of miRNA-induced repression (Fig. 2F). These data indicate that the increased availability of miR-15/16 leads to increased repression of mRNA target genes when Malat1:miR-15/16 interaction is ablated.

We further investigated genes that displayed reciprocal expression changes in miR-15/16$^{\Delta/\Delta}$ and *Malat1*$^{scr/scr}$ cells. Of 479 genes in the bound target list, 432 (90%) were either downregulated in *Malat1*$^{scr/scr}$ cells or upregulated in miR-15/16$^{\Delta/\Delta}$ cells, compared to controls. Among these genes, the expression of 298 (62%) were decreased in *Malat1*$^{scr/scr}$ cells, and 294 (61%) were increased in miR-15/16$^{\Delta/\Delta}$ cells, with 160 (33%) both increased in miR-15/16$^{\Delta/\Delta}$ and decreased in *Malat1*$^{scr/scr}$ cells (Fig 2G). Gene ontology enrichment analysis revealed multiple pathways associated with growth factor and antigen receptor signaling affected by the Malat1:miR-15/16 circuit in cytotoxic T cells (Fig. 2H). Many of these modules, including the T cell activation module, were identified because they share key signaling proteins. For example, gene expression and AHC data support direct miR-15/16 targeting of the costimulatory receptor *Cd28,* the alpha subunit of phosphatidylinositol 3-kinase (*Pik3r1*) and c-Jun N-terminal kinase (JNK1), encoded by *Mapk8* (Fig. S2 and Fig. 3). Targeting of these genes by miR-15/16 is consistent with their known tumor suppressor role (Cimmino

et al., 2005; Gagnon et al., 2019) and with Malat1's association with cancer cell proliferation and metastasis (Ji et al., 2003), providing new mechanistic insight into those observations.

Figure 2. Malat1 Inhibits miR-15/16 binding and suppressive activity

(A) Malat1 expression measure by RNA-seq from CD8+ T cells isolated from spleens and stimulated with αCD3 and αCD28 for 24 hours (WT n = 6, *Malat1*$^{scr/scr}$ n = 7, miR-15/16$^{fl/fl}$ n = 6, miR-15/16$^{\Delta/\Delta}$ n = 6; 1 experiment)

(B) miR-16, miR-15b, and miR-15a expression measured by miRNA qPCR from CD8^{+} T cells freshly isolated from spleens. Expression was determined relative to 5.8s ribosomal RNA expression. Unpaired t-test performed to determine significance.

(C-D) TargetScan predicted miR-15/16 binding sites that contained at least one HITS-CLIP read in both WT and *Malat1*$^{scr/scr}$ CD8^{+} T cells were compared for depth of Ago2 HITS-CLIP reads. First, reads at the predicted seed site were normalized by total Ago2 HITS-CLIP reads in a given 3' UTR. To best visualize all sites, logit transforms of these values are plotted. Paired t-test performed to determine significance. Blue line indicates the identity line. Data for each genotype is from combined libraries of n = 2 biological replicates.

(C) Comparison of WT and *Malat1*$^{scr/scr}$ cells

(D) Comparison of WT and miR-15/16$^{\Delta/\Delta}$. Values to the left of the y-axis labeled with NB indicate there was no bind detected at that site in the miR-15/16$^{\Delta/\Delta}$ cells.

(E-F) Cumulative density plots to determine changes in expression of miR-15/16 targets. Targets determined by TargetScan predicted miR-15/16 mRNA targets that had at least one 3' UTR site with reads in both WT and Malat1$^{scr/scr}$ CD8^{+} T cells. Kolmogorov-Smirnov test used to determine significant differences in the distributions of target and non-target genes.

(E) comparison of the Log_2(FC) between WT and *Malat1*$^{scr/scr}$ samples stimulated with αCD3 and αCD28 for 24 hours

(F) comparison of the Log_2(FC) between miR-15/16$^{fl/fl}$ and miR-15/16$^{\Delta/\Delta}$ samples stimulated with αCD3 and αCD28 for 24 hours.

(G) Venn diagram of miR-15/16 target expression regulated in concordance with the Malat1-miR-15/16 circuit. The blue circle indicates genes with WT vs *Malat1*$^{scr/scr}$ $log_2(FC) > 0$ and the red circle indicates genes with miR-15/16$^{fl/fl}$ vs miR-15/16$^{\Delta/\Delta}$ $log_2(FC) < 0$. The purple overlap indicates genes that meet both conditions and the grey indicates genes that do not meet either condition.

(H) Gene ontology analysis of the bound target set used above as well as genes regulated in accordance with the Malat1-miR-15/16 circuit (WT vs *Malat1*$^{scr/scr}$ $log_2(FC) > 0$ or miR-15/16$^{fl/fl}$ vs miR-15/16$^{\Delta/\Delta}$ $log_2(FC) < 0$). Enrichment determined within the Panther Pathway annotations.

(*, $p<0.05$)

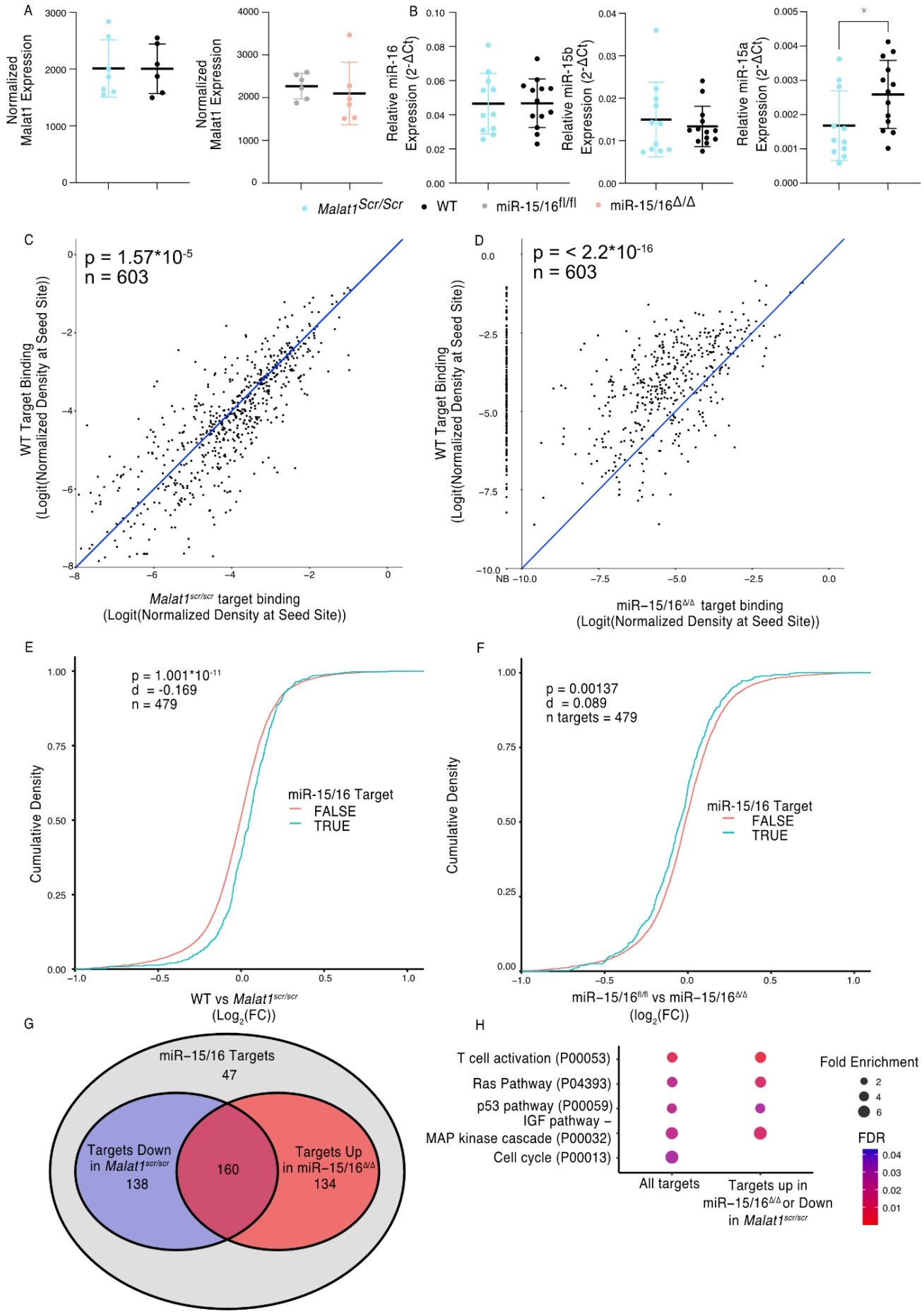
A
Normalized Malat1 Expression
B
Relative miR-16 Expression (2^-ΔCt)
Relative miR-15b Expression (2^-ΔCt)
Relative miR-15a Expression (2^-ΔCt)
Malat1Scr/Scr
WT
miR-15/16fl/fl
miR-15/16Δ/Δ
C
p = 1.57*10-5
n = 603
WT Target Binding (Logit(Normalized Density at Seed Site))
Malat1scr/scr target binding (Logit(Normalized Density at Seed Site))
D
p = < 2.2*10-16
n = 603
WT Target Binding (Logit(Normalized Density at Seed Site))
miR−15/16Δ/Δ target binding (Logit(Normalized Density at Seed Site))
E
p = 1.001*10-11
d = -0.169
n = 479
Cumulative Density
miR-15/16 Target
FALSE
TRUE
WT vs Malat1scr/scr (Log2(FC))
F
p = 0.00137
d = 0.089
n targets = 479
Cumulative Density
miR-15/16 Target
FALSE
TRUE
miR−15/16fl/fl vs miR−15/16Δ/Δ (log2(FC))
G
miR−15/16 Targets
47
Targets Down in Malat1scr/scr
138
160
Targets Up in miR−15/16Δ/Δ
134
H
T cell activation (P00053)
Ras Pathway (P04393)
p53 pathway (P00059)
IGF pathway –
MAP kinase cascade (P00032)
Cell cycle (P00013)
All targets
Targets up in miR−15/16Δ/Δ or Down in Malat1scr/scr
Fold Enrichment
FDR

Malat1 enhances CD28 Expression and Downstream CD8 T Cell Activation

Given that the Malat1:miR-15/16 circuit regulated genes essential to T cell activation, and in particular CD28, we next investigated the functional consequences of perturbing this circuit in cytotoxic T cells. First, we looked directly at CD28. AHC in WT cells detected a prominent peak in the CD28 3'UTR at the TargetScan predicted binding site for miR-15/16. This peak was absent in miR-15/16$^{\Delta/\Delta}$ cells, whereas other binding peaks were preserved, empirically verifying that this binding event is miR-15/16-dependent. AHC in *Malat1*$^{scr/scr}$ cells indicated a modest increase in Ago2 binding at this site compared to WT cells relative to Ago2 binding in the whole 3' UTR (Fig 3A). These data, along with our previous demonstration that the CD28 3' UTR is miR-15/16 responsive, indicates that CD28 is part of a module of miR-15/16 target genes that are highly likely to be affected by the *Malat1*^{scr} allele (Gagnon et al., 2019).

Indeed, CD28 expression and T cell activation were regulated by the Malat1:miR-15/16 circuit. Flow cytometric measurement in primary splenic CD8^{+} T cells revealed that CD28 protein expression was decreased in *Malat1*$^{scr/scr}$ mice and enhanced in miR-15/16$^{\Delta/\Delta}$ mice (Fig 3B-C). To investigate activation-induced gene expression, we performed RNA-seq on splenic CD8^{+} T cells stimulated for 24 hours with plate-bound αCD3 with or without αCD28 cross-linking antibodies diagrammed in (Figure 3D). CD28 stimulation enhances distinct activation-induced gene expression changes in T cells (Martínez-Llordella et al., 2013), and these CD28-responsive genes were altered in miR-15/16$^{\Delta/\Delta}$ and *Malat1*$^{scr/scr}$ cells (Fig 3E-H). The previously defined set of 164 genes that are upregulated in WT cells stimulated with αCD3 + αCD28 compared to αCD3 alone was also significantly upregulated in the αCD3 + αCD28 condition compared to αCD3 alone for each genotype tested in our experiments (Fig S3A-D). Importantly, the Malat1:miR-15/16 circuit affected this gene set in the αCD3 alone condition, with Malat1$^{scr/scr}$ cells exhibiting decreased expression compared to WT cells, and miR-15/16$^{\Delta/\Delta}$ cells exhibiting increased expression compared to miR-15/16$^{fl/fl}$ cells (Fig 3E,G). This trend was preserved, but to a lesser degree, in the αCD3 and αCD28 condition (Fig 3 F,H). Thus, Malat1:miR-15/16 interaction enhanced expression of a costimulation-responsive gene expression program in activated T cells, and it further enhanced expression of that module even when CD28 costimulation was directly engaged.

Unsupervised hierarchical clustering of these samples based on the expression of the 164 costimulation-responsive gene set further underscored the costimulatory-like effect of the Malat1:miR-15/16 circuit. In comparing gene expression in *Malat1*$^{scr/scr}$ and WT samples, 3 major groups emerged. The group with the lowest average costimulation-responsive gene expression contained only samples stimulated with αCD3 alone and primarily *Malat1*$^{scr/scr}$ samples. The group with intermediate expression was the largest group with an even representation of *Malat1*$^{scr/scr}$ samples and WT samples. While samples in this intermediate group were from both stimulation conditions, the *Malat1*$^{sc/scr}$ samples tended to be from the αCD3 + αCD28 condition and the WT samples had an even representation from both stimulation conditions. The group with the highest average expression contained predominantly αCD3 + αCD28 stimulated samples with an even representation of *Malat1*$^{scr/scr}$ and WT samples (Fig 3I). Thus, Malat1:miR-15/16 interaction and engagement of CD28 signaling additively induced costimulation-responsive genes. This observation is further supported when clustering the miR-15/16$^{\Delta/\Delta}$ and miR-15/16$^{fl/fl}$ samples. The 2 largest clusters were divided nearly exclusively by genotype. The group with lower average expression of costimulation-responsive genes contained predominantly mir-15/16$^{fl/fl}$ samples stimulated with αCD3 alone. The group with the higher average expression contained a majority of miR-15/16$^{\Delta/\Delta}$ samples, and the only miR-15/16$^{fl/fl}$ samples within the group received αCD3 + αCD28 stimulation. Within the higher expression group, the miR-15/16$^{fl/fl}$ samples stimulated with αCD3 + αCD28 sub-clustered with miR-15/16$^{\Delta/\Delta}$ samples stimulated with αCD3 alone (Fig 3J). A third, much smaller cluster was composed of both samples from a single outlier biological replicate. Overall, these data show that miR-15/16 restrict costimulation-responsive gene expression, and that Malat1:miR-15/16 interaction limits this effect.

In addition to the proximal changes in gene expression, downstream functional outcomes of CD28 costimulation were also affected. Early activation genes have been well described in T cells, with CD69

responding to many cues including TCR and CD28 ligation, and Nur77 responding very specifically to TCR signals (Ashouri and Weiss, 2017; Vandenberghe et al., 1993). In similar fashion as above, we assessed the expression of these proteins 2 and 4 hours after stimulation with plate bound cross linking antibodies on primary CD8+ T cells. CD69 exhibited decreased expression in *Malat1*$^{scr/scr}$ cells at both 2 and 4 hours post stimulation (2 hr: $p=0.0014$ and 4 hr: $p=0.0598$) and increased expression in miR-15/16$^{\Delta/\Delta}$ cells at 4 hours post stimulation only ($p < 0.0001$) (Fig 4 A-B), in accordance with costimulation-responsive gene module expression (Fig 3). There was no difference, however, in expression of Nur77 across *Malat1*$^{scr/scr}$, WT, and miR-15/16$^{\Delta/\Delta}$ cells, indicating that TCR signals were equivalent (Fig 4 A,C). Another key consequence of CD28 ligation is the production of IL-2 (Fraser et al., 1991; Maggirwar et al., 1997; Vandenberghe et al., 1993). Therefore, we assessed cytokine production in the supernatants of these cultures 16 hours after stimulation. In line with previous findings in LCMV-infected mice (Gagnon et al., 2019), miR-15/16$^{\Delta/\Delta}$ cells made significantly more IL-2 and TNFα after αCD3 stimulation both with and without αCD28, with a trend toward increased IFNɣ as well (Fig 4D-F). Malat1$^{scr/scr}$ cells stimulated with αCD3+αCD28 exhibited a reciprocal trend specifically for IL-2 (23% decrease compared to WT, $p=0.26$) (Fig 4D). Together, these data show that the Malat1:miR-15/16 circuit regulates key functional outcomes of CD28-mediated costimulation, from proximal gene expression changes to early activation protein expression and cytokine secretion.

Figure 3. The Malat1-miR-15/16 Circuit Increase CD28 Expression and Co-stimulation induced Gene Expression

(A) Ago2 HITS-CLIP binding at the Cd28 locus. Sequencing libraries generated from $CD8^+$ T cells isolated from spleens and cultured for 5 days (combined libraries from n = 2 for each genotype). Grey bar indicates the peak containing the TargetScan predicted miR-15/16 binding site.

(B) Schematic illustrating the assay scheme to assay acute gene expression downstream of CD28 co-stimulation

(C) Representative flow cytometry plots of CD28 expression on naive ($CD62L^+$ $CD44^-$) CD8+ T cells from spleens of unchallenged mice. Mean fluorescence intensity for the sample reported in the upper right of the plot.

(D) Quantification of CD28 mean fluorescence intensity normalized to the relevant control. (*Malat1*$^{scr/scr}$ compared to WT from 3 independent experiments; miR-15/16$^{fl/fl}$ compared to miR-15/16$^{\Delta/\Delta}$ from 2 independent experiments)

(E-H) Cumulative density plots comparing expression of CD28 responsive gene set defined as genes from (Martínez-Llordella et al., 2013) with αCD3αCD28 vs αCD3 $\log_2$(FC) > 1.5 and adjusted p value < 0.001. Kolmogorov-Smirnov test used to determine significant differences in the distributions of target and non-target genes. αCD3 used at 1 µg/mL, and α CD28 used at 1 µg/mL.

(E) Comparison of CD28 responsive genes in WT vs *Malat1*$^{scr/scr}$ cells stimulated with αCD3 alone

(F) Comparison of CD28 responsive genes in WT vs *Malat1*$^{scr/scr}$ cells stimulated with αCD3 and αCD28

(G) Comparison of CD28 responsive genes in miR-15/16$^{fl/fl}$ vs miR-15/16$^{\Delta/\Delta}$ cells stimulated with αCD3 alone

(H) Comparison of CD28 responsive genes in miR-15/16$^{fl/fl}$ vs miR-15/16$^{\Delta/\Delta}$ cells stimulated with αCD3 and αCD28

(I-J) Heatmaps of CD28 responsive gene set expression by genotype and stimulation condition. Dendrograms represent unbiased hierarchical clustering of the samples.

(I) *Malat1*$^{scr/scr}$ and WT samples compared with αCD3 ± αCD28

(J) miR-15/16$^{fl/fl}$ vs miR-15/16$^{\Delta/\Delta}$ samples compared with αCD3 ± αCD28

(*, p<0.05; **, p<0.01;***,p<0.001; ****, p<0.0001)

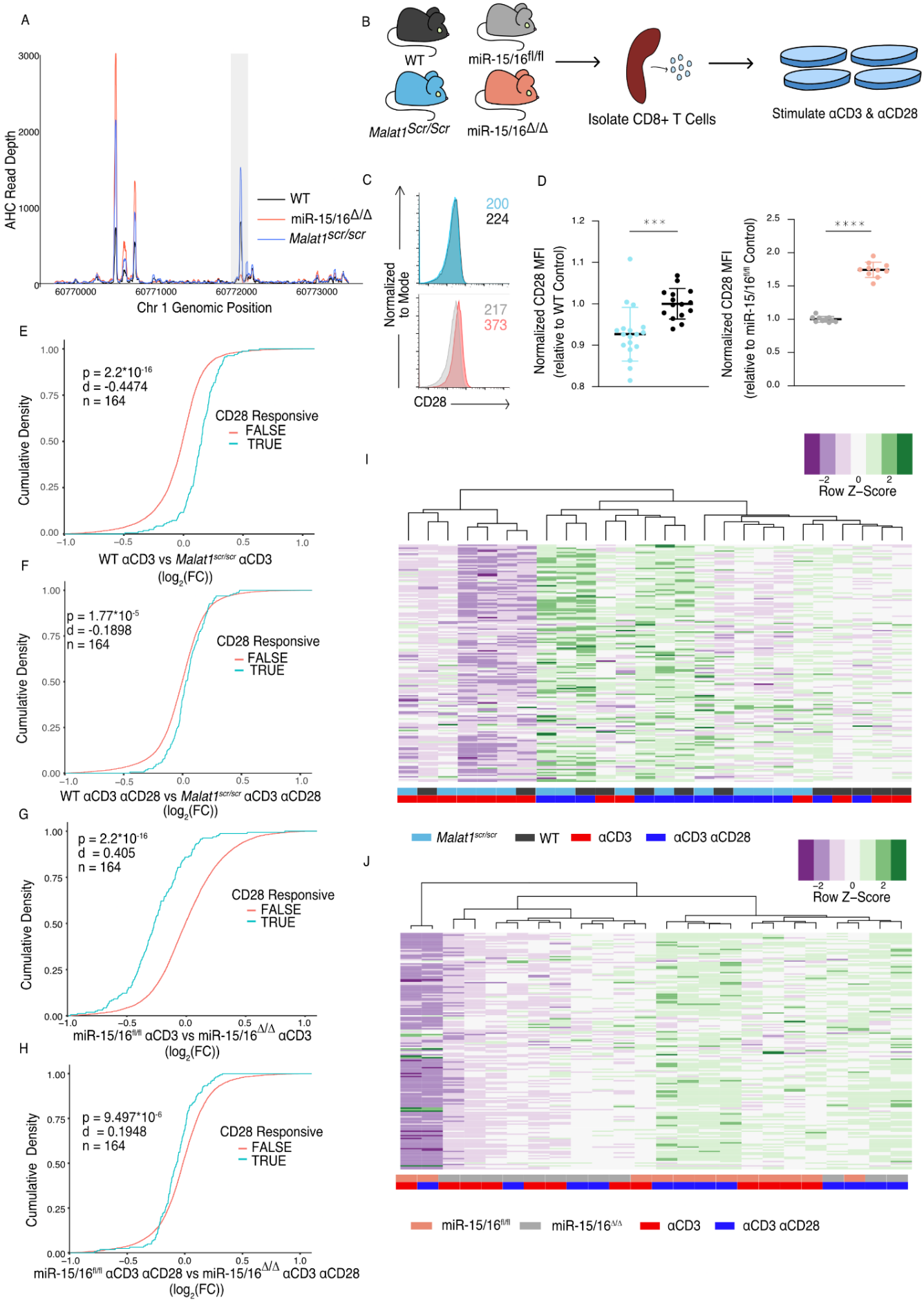
A
AHC Read Depth
Chr 1 Genomic Position
WT
miR-15/16Δ/Δ
Malat1scr/scr
B
WT
miR-15/16fl/fl
Malat1Scr/Scr
miR-15/16Δ/Δ
Isolate CD8+ T Cells
Stimulate αCD3 & αCD28
C
200
224
217
373
Normalized to Mode
CD28
D
Normalized CD28 MFI (relative to WT Control)
Normalized CD28 MFI (relative to miR-15/16fl/fl Control)
E
p = 2.2*10-16
d = -0.4474
n = 164
CD28 Responsive
FALSE
TRUE
Cumulative Density
WT αCD3 vs Malat1scr/scr αCD3 (log2(FC))
F
p = 1.77*10-5
d = -0.1898
n = 164
WT αCD3 αCD28 vs Malat1scr/scr αCD3 αCD28 (log2(FC))
G
p = 2.2*10-16
d = 0.405
n = 164
miR-15/16fl/fl αCD3 vs miR-15/16Δ/Δ αCD3 (log2(FC))
H
p = 9.497*10-6
d = 0.1948
n = 164
miR-15/16fl/fl αCD3 αCD28 vs miR-15/16Δ/Δ αCD3 αCD28 (log2(FC))
I
Row Z-Score
Malat1scr/scr
WT
αCD3
αCD3 αCD28
J
Row Z-Score
miR-15/16fl/fl
miR-15/16Δ/Δ
αCD3
αCD3 αCD28

Figure 4. The Malat1-MiR-15/16 circuit increases functional outcomes of CD28 co-stimulation

(A-C) $CD8^+$ T cells were isolated from spleens and stimulated with αCD3 and αCD28 antibodies, results displayed are gated on activated cells ($CD69^+$ $Nur77^+$)

(A) Representative histograms of CD69 and Nur77 expression 4 hours after stimulation

(B) Quantification of CD69 mean fluorescence intensity 2 and 4 hours after stimulation. Both time points reflect statistically significant changes ($p < 0.01$) by ordinary one-way ANOVA; statistics displayed on graph represent results of post-hoc multiple comparisons of *Malat1*$^{scr/scr}$ to WT and miR-15/16$^{\Delta/\Delta}$ to WT. Data from 2 independent experiments, each normalized to WT average value.

(C) Quantification of Nur77 mean fluorescence intensity 2 and 4 hours after stimulation. No significant changes determined by ordinary one-way ANOVA. Data from 2 independent experiments, each normalized to WT average value.

(D-F) Quantification of cytokine secretion into the supernatant by $CD8^+$ T cells isolated from spleens, stimulated αCD3 ± αCD28, and cultured 16 hours. Cell free supernatant protein concentration measured by ELISA. Data from a single experiment

(D) Quantification of IL-2 secretion. By 2-way ANOVA, in both experiments there was a significant ($p < 0.0001$) increase in IL-2 with the addition of αCD28 stimulation. But the only significant ($p = 0.0001$) genotypic effect was increased IL-2 secretion in miR-15/16$^{\Delta/\Delta}$ vs mir-15/16$^{fl/fl}$. Comparisons shown on plot are the results of post-hoc multiple comparison tests.

(E) Quantification of TNFα secretion. By 2-way ANOVA, in both experiments there was a significant ($p < 0.0001$) increase in IL-2 with the addition of αCD28 stimulation. But the only significant ($p = 0.003$) genotypic effect was increased IL-2 secretion in miR-15/16$^{\Delta/\Delta}$ vs mir-15/16$^{fl/fl}$. Comparisons shown on plot are the results of post-hoc multiple comparison tests.

(F) Quantification of IFNɣ secretion. By 2-way ANOVA, in both experiments there was a significant ($p < 0.0001$) increase in IL-2 with the addition of αCD28 stimulation. But no genotypic effect was observed.

(*, $p<0.05$; **, $p<0.01$;***,$p<0.001$; ****, $p<0.0001$)

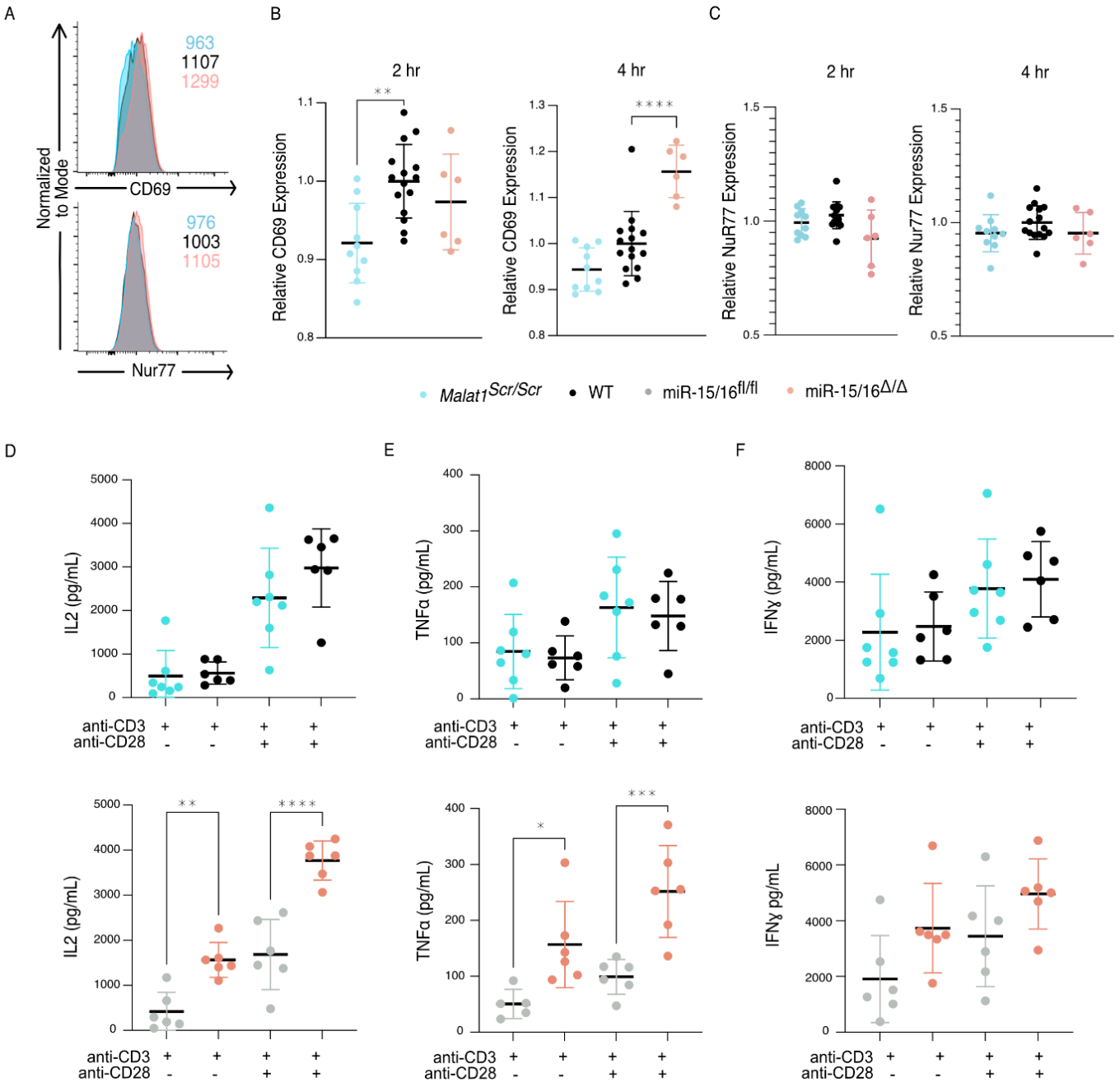
A
963
1107
1299
Normalized to Mode
CD69
976
1003
1105
Nur77
B
2 hr
4 hr
Relative CD69 Expression
**
****
C
Relative NuR77 Expression
Relative Nur77 Expression
Malat1Scr/Scr
WT
miR-15/16fl/fl
miR-15/16Δ/Δ
D
E
F
IL2 (pg/mL)
TNFα (pg/mL)
IFNγ (pg/mL)
IFNγ pg/mL
anti-CD3
anti-CD28
*
***

Malat1 enhances Cytotoxic Memory T Cell Differentiation

miR-15/16 restrict memory T cell differentiation, cell cycle, and cell survival during the response to LCMV Armstrong infection (Gagnon et al., 2019). CD28 costimulation is essential for IL-2 production, memory cell formation, and memory recall responses *in vivo* (Borowski et al., 2007; Eberlein et al., 2012-2; Fuse et al., 2008; Grujic et al., 2010; Suresh et al., 2001). IL-2 is also essential for these same processes and in particular is required in a $CD8^+$ T cell intrinsic nature for the formation of $CD127^+$ $KLRG1^-$ memory cells (Blattman et al., 2003; Kahan et al., 2022; Pipkin et al., 2010; Toumi et al., 2022; Whyte et al., 2022). Since Malat1 inhibits miR-15/16 activity and this circuit impacts proper T cell activation and IL-2 production after CD28 costimulation, we hypothesized that *Malat1*$^{scr/scr}$ cells would exhibit poor memory formation and survival.

We first examined steady state memory populations of polyclonal T cells in unchallenged, young mice. *Malat1*$^{scr/scr}$ mice had normal naive and central memory T cell populations, but a reduced percentage and number of effector memory ($CD44^+CD62L^-$) cells in the spleen (Fig S4). Therefore, we investigated the cell intrinsic nature of the *Malat1*$^{scr/scr}$ memory cell impairment during a viral challenge known to induce a large memory response. We bred the *Malat1*$^{scr/scr}$ mice with P14 TCR transgenic mice that express an antigen receptor specific for the immunodominant LCMV GP33 peptide. We then transferred *Malat1*$^{scr/scr}$ and WT P14 T cells into congenic CD45.1 hosts followed by LCMV Armstrong infection and tracked the acute and memory responses in the spleen and liver, the sites of primary LCMV infection (Figure 5A) (Matloubian et al., 1993).

The total numbers of P14 cells were similar in recipients of transferred WT or *Malat1*$^{scr/scr}$ P14 cells in both the spleen and liver at day 7, and in the spleen at day 31. However, there was a reduction in *Malat1*$^{scr/scr}$ P14 cells in the liver at day 31 (Fig 5 B-C). Despite having no effect on cell expansion at the peak of infection and mixed cell number results in the memory phase, the *Malat1*^{scr} allele had a distinct effect on the cellular phenotype across organs and time points. *Malat1*$^{scr/scr}$ P14 cells preferentially displayed a phenotype associated with terminally differentiated effector memory cells (t-TEM), defined by KLRG1 expression and lack of CD127 expression as shown by (Milner et al., 2020), and a corresponding reduction in the percentage of $KLRG1^-$ $CD127^+$ memory cells (Fig 5 D-F). Previous work has shown that substantial heterogeneity exists in the memory pool and that CD27 and CD43 can be useful in delineating functional differences such as recall potential between different memory cells. For instance, $CD27^+$ memory cells tend to produce more IL-2 than $CD27^-$ cells (Milner et al., 2020), and $CD43^+$ $CD27^+$ cells are more effective at clearing Listeria upon re-challenge (Hikono et al., 2007; Olson et al., 2013). We therefore assessed these markers on the transferred *Malat1*$^{scr/scr}$ and WT P14 cells. Consistent with increased $KLRG1^+$ $CD127^-$ t-TEM cells there were proportionally more $CD27^-$ $CD43^-$ cells in both the spleen and liver at day 31 among the *Malat1*$^{scr/scr}$ transferred cells compared to WT (Fig 5 G,I). $CD27^+$ $CD43^-$ cells were unchanged. The proportional reduction in $CD127^+$ $KLRG1^-$ cells corresponded with a decreased proportion of $CD43^+$ $CD27^+$ cells. Notably, the total numbers of all $CD27^-$ subsets were unchanged. The proportional differences we observed were primarily driven by a reduction in the number of $CD43^+$ $CD27^+$ *Malat1*$^{scr/scr}$ P14 cells compared with wild type P14 cells (45% reduction in liver ($p = 0.0058$), 30% reduction in spleen ($p = 0.113$)) (Fig 5 G-I). This phenotype is exactly reciprocal to the increase in $CD27^+$ memory cells previously documented in miR-15/16$^{\Delta/\Delta}$ mice (Gagnon et al., 2019). To test whether the effect of the *Malat1*^{scr} allele was epistatic to miR-15/16, we bred *Malat1*$^{scr/scr}$ mice to miR-15/16$^{\Delta/\Delta}$ mice to generate triple mutant *Malat1*$^{scr/scr}$ miR-15/16$^{\Delta/\Delta}$ mice. The poly-clonal LCMV response in these mice phenocopied that of miR-15/16$^{\Delta/\Delta}$ with a WT allele of Malat1, indicating that the observed effects of the *Malat1*^{scr} allele are epistatic to miR-15/16 (Fig S5). We conclude that Malat1 inhibits miR-15/16 in responding $CD8^+$ T cells during LCMV infection, leading to fewer $CD43^+$ $CD27^+$ memory cells.

Compared to LCMV, *Listeria monocytogenes* (LM) infection induces lower expression of multiple co-stimulatory ligands so the antigen specific response is more sensitive to the ablation of CD28 co-stimulation (Welten et al., 2015). Therefore, we hypothesized that cytotoxic T cell response may be more impaired by the *Malat1*^{scr} allele during LM infection. We first sought to understand the effect of miR-15/16 on cytotoxic T cells during primary LM infection. To do so, we directly infected polyclonal mir-15/16$^{fl/fl}$ and miR-15/16$^{\Delta/\Delta}$ mice with

LM expressing the LCMV GP33 peptide (LM-GP33) (Fig 6A). In contrast to the increased antigen-specific $CD8^+$ T cell numbers in LCMV-infected miR-15/16$^{\Delta/\Delta}$ mice (Gagnon et al., 2019), we observed similar cell numbers in LM-GP33 infected miR-15/16$^{\Delta/\Delta}$ and miR-15/16$^{fl/fl}$ mice (Fig 6B). However, the effect on memory cell differentiation was still present with decreased percentages of $CD127^-$ $KLRG1^+$ t-TEMs and increased percentages of $CD127^+$ $KLRG1^-$ memory cells (Fig 6 C,D). Again, miR-15/16$^{\Delta/\Delta}$ antigen specific cells had a significantly lower proportion of $CD43^-$ $CD27^-$ cells and a trend toward proportionally more $CD43^+$ $CD27^+$ cells ($p = 0.127$) (Fig 6 E,F).

Given that antigen-specific miR-15/16$^{\Delta/\Delta}$ T cells exhibited enhanced memory cell differentiation during LM-GP33 infection, we further tested the role of Malat1:miR-15/16 interaction in this model using the P14 adoptive transfer system (Fig 6F). Transferred *Malat1*$^{scr/scr}$ and WT P14 cells accumulated in the spleen and the liver to similar numbers at both day 7 and day 31 following LM-GP33 infection (Fig 6H). In contrast to LCMV, there was no change in the proportion or number of $CD127^-$ $KLRG1^+$ *Malat1*$^{scr/scr}$ P14 cells at day 7 in the spleen or liver (Fig 6I). However, in LM-GP33 infection at day 7, CD43 and CD27 expression didn't explicitly mirror the phenotype observed by CD127 and KLRG1 expression. In the spleen, there was a proportional and numerical increase in $CD43^-$ $CD27^-$ P14 cells with the *Malat1*$^{scr/scr}$ genotype (Fig 6J). There was a decreased proportion of $CD43^+$ $CD27^+$ cells ($p = 0.0531$), but this was despite a trend towards increased numbers of these cells ($p = 0.1056$) in the *Malat1*$^{scr/scr}$ P14 cells (Fig 6K). In the liver, there were no significant trends in any of these populations at day 7 (Fig 6 J,K).

Although some of the phenotypes observed with LCMV were attenuated or absent during acute infection with LM-GP33 at day 7, Malat1:miR-15/16 interaction had more pronounced effects on memory cell populations at later times post-infection (Fig 6 L,M). On day 31, $KLRG1^+$ cells were increased in proportion and numbers in the *Malat1*$^{scr/scr}$ P14 cells (Fig 6N). In the liver, a similar trend in $KLRG1^+$ cell proportion existed ($p = 0.233$), but the numeric effect was entirely absent (Fig 6N). Surprisingly, this effect was restricted to the $KLRG1^+$ populations, as $CD127^+$ $KLRG1^-$ memory cells were unaffected in proportion and number in both the spleen and liver (Fig 6O). In both organs $CD43^-$ $CD27^-$ t-TEMs were proportionally increased and $CD43^+$ $CD27^+$ memory cells were proportionally decreased in *Malat1*$^{scr/scr}$ P14 cells (Fig 6P,Q). The numeric underpinnings of these proportional changes were different in each organ, with a 94% increase in $CD43^-$ $CD27^-$ cells in the spleen, and a 40% loss of the $CD43^+$ $CD27^+$ population in the liver (Fig 6P,Q). Taken together, these data demonstrate that miR-15/16 restrict memory cell differentiation, and reveal the ability of Malat1:miR-15/16 interaction to enhance memory cell differentiation across infection contexts.

Figure 5. Malat1 enhances memory T cell persistence following LCMV infection

Malat1$^{scr/scr}$ and WT cells containing the GP33 specific TCR transgene (P14) on the CD45.2 background were transferred separately into congenic CD45.1 WT hosts. One day later the recipient mice were infected with $5*10^5$ p.f.u. I.p. lcmv armstrong. LCMV specific responses were assayed by monitoring the transferred cells by flow cytometry in the blood, spleen, and liver over time (data from two independent experiments per time point)

(A) Schematic of experimental design

(B) Representative flow plots to identify and quantify transferred cells

(C) Quantification of transferred P14 cell numbers at day 7 and day 31

(D) Representative flow plots of KLRG1 and CD127 expression on P14 cells at day 31 post infection

(E) Quantification of P14 KLRG1$^+$ cells by percent of P14 and total numbers in spleen and liver at day 7 and day 31 post infection

(F) Quantification of P14 KLRG1$^-$ CD127$^+$ by percent of P14 and total numbers in spleen and liver at day 31 post infection

(G) Representative flow plots of CD43 and CD27 expression on P14 cells at day 31 post infection

(H) Quantification of P14 CD43$^-$ CD27$^-$ t-Tem cells by percent of P14 and total numbers in spleen and liver at day 31 post infection

(I) Quantification of P14 CD43$^+$ CD27$^+$ memory cells by percent of P14 and total numbers in spleen and liver at day 31 post infection

Statistics displayed determined by unpaired t-test between *Malat1*$^{scr/scr}$ and WT transferred cells (*, $p<0.05$; **, $p<0.01$)

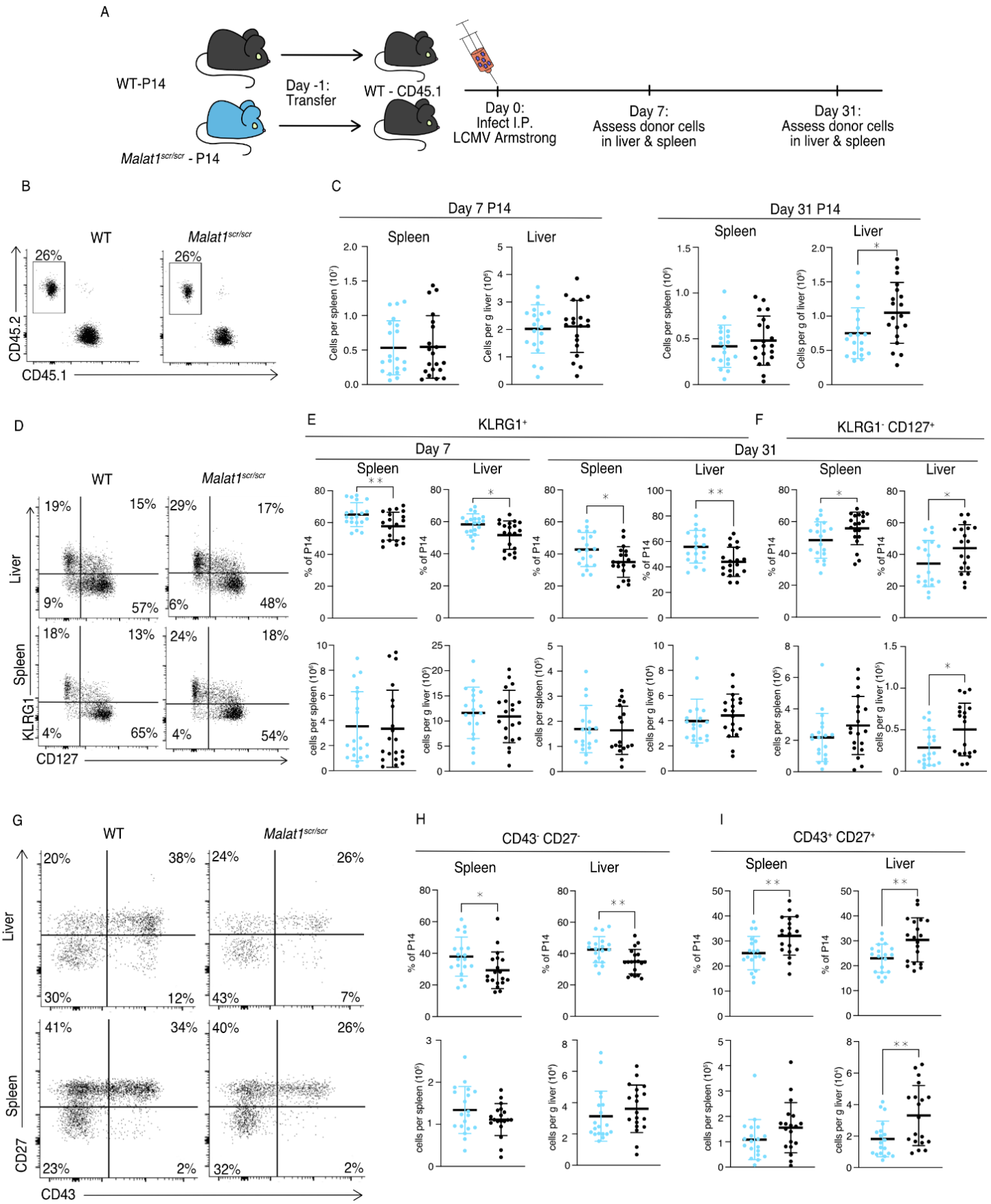
A
WT-P14
Malat1scr/scr - P14
Day -1: Transfer
WT - CD45.1
Day 0: Infect I.P. LCMV Armstrong
Day 7: Assess donor cells in liver & spleen
Day 31: Assess donor cells in liver & spleen
B
WT
Malat1scr/scr
26%
26%
CD45.2
CD45.1
C
Day 7 P14
Spleen
Liver
Cells per spleen (10^7)
Cells per g liver (10^6)
Day 31 P14
Spleen
Liver
Cells per spleen (10^6)
Cells per g of liver (10^6)
D
WT
Malat1scr/scr
Liver
Spleen
KLRG1
CD127
19%
15%
9%
57%
29%
17%
6%
48%
18%
13%
4%
65%
24%
18%
4%
54%
E
KLRG1+
Day 7
Spleen
Liver
Day 31
Spleen
Liver
% of P14
cells per spleen (10^6)
cells per g liver (10^6)
F
KLRG1- CD127+
Spleen
Liver
G
WT
Malat1scr/scr
Liver
Spleen
CD27
CD43
20%
38%
30%
12%
24%
26%
43%
7%
41%
34%
23%
2%
40%
26%
32%
2%
H
CD43- CD27-
Spleen
Liver
% of P14
cells per spleen (10^6)
cells per g liver (10^4)
I
CD43+ CD27+
Spleen
Liver
% of P14
cells per spleen (10^6)
cells per g liver (10^4)

Figure 6. Malat1 and miR-15/16 alter memory T cell differentiation following *Listeria Monocytogenes* infection

miR-15/16$^{fl/fl}$ and miR-15/16$^{\Delta/\Delta}$ with a polyclonal TCR repertoire were directly infected with $2*10^4$ colony forming units (c.f.u.) r.o. *Listeria monocytogenes-gp33* (LM-GP33). LM-GP33 specific responses were then assayed in the spleen 31 days post infection (miR-15/16$^{\Delta/\Delta}$ n = 5 and miR-15/16$^{fl/fl}$ n = 6 from a single experiment).

(A) schematic of experimental design

(B) Quantification of tetramer specific CD8 T cells in the spleen

(C-F) Quantification of tetramer specific subpopulations by percent of GP33+ and numbers for (C) CD127$^-$ KLRG1$^-$, (D) CD127$^+$ KLRG1$^-$, (E) CD27$^-$ CD43$^-$, and (F) CD27$^+$ CD43$^+$ populations

Malat1$^{scr/scr}$ and WT cells containing the GP33 specific TCR transgene (P14) on the CD45.2 background were transferred separately into congenic CD45.1 WT hosts. One day later the recipient mice were infected with $2*10^4$ c.f.u. r.o. LM-GP33. LM-GP33 specific responses were assayed by monitoring the transferred cells by flow cytometry in the spleen and liver at discrete time points (data from a single experiment per time point).

(G) Schematic of experimental design

(H) Quantification of transferred P14 cell numbers at day 7 and day 31

(I-K) Quantification of P14 (I) CD127$^-$ KLRG1$^+$, (J) CD43$^-$ CD27$^-$, and (K) CD43$^+$ CD27$^+$ cells by percent of P14 and total numbers in spleen and liver at day 7

(L) Representative flow plots of KLRG1 and CD127 expression on P14 cells at day 31 post infection

(M) Representative flow plots of CD43 and CD27 expression on P14 cells at day 31 post infection

(N-Q) Quantification of P14 (N) KLRG1$^+$, (O) CD127$^+$ KLRG1$^-$, (P) CD43$^-$ CD27$^-$, and (Q) CD43$^+$ CD27$^+$ cells by percent of P14 and total numbers in spleen and liver at day 31 post infection

Statistics displayed determined by unpaired t-test between *Malat1*$^{scr/scr}$ and WT transferred cells (*, $p<0.05$; **, $p<0.01$;***,$p<0.001$)

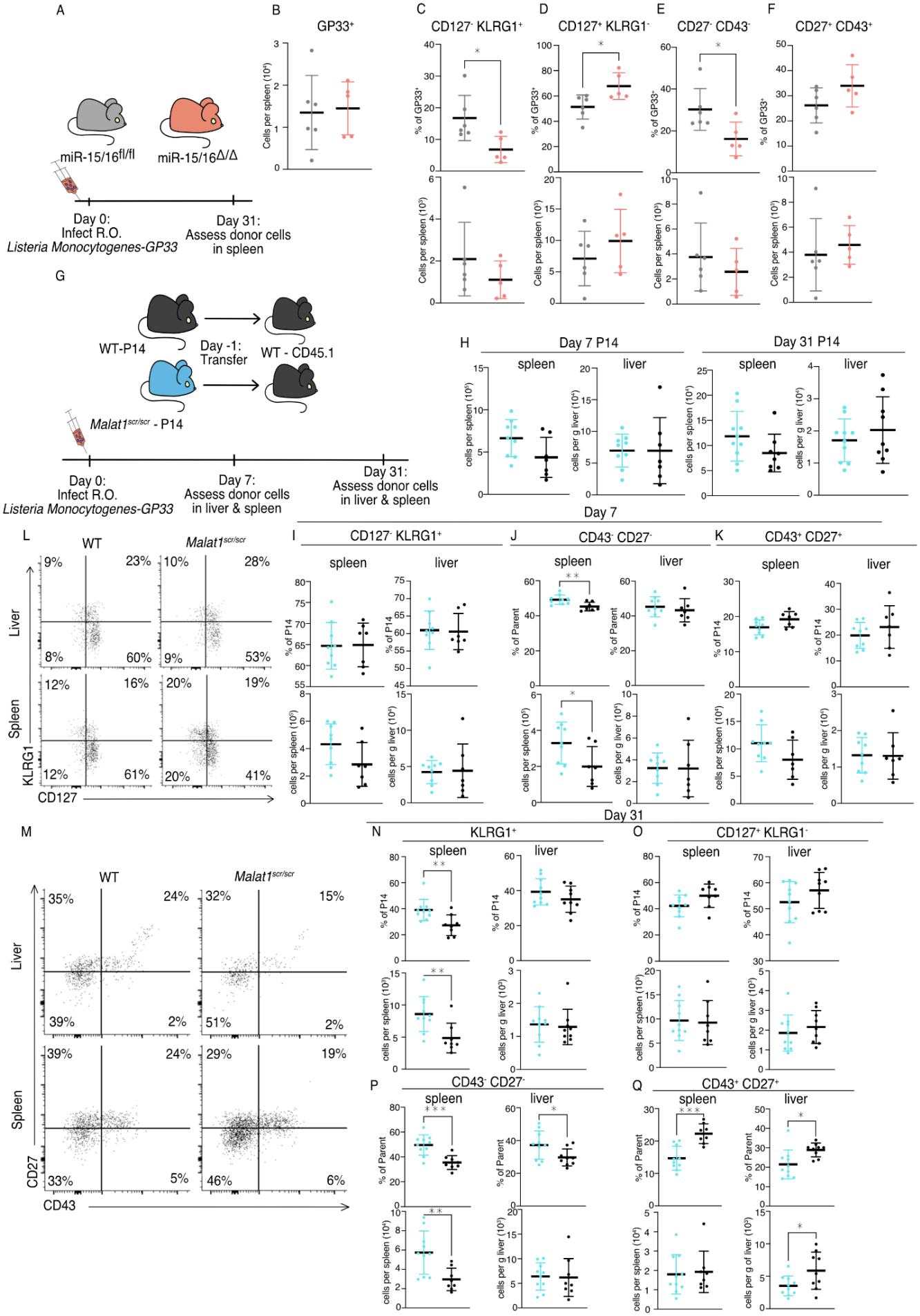
A
miR-15/16fl/fl
miR-15/16Δ/Δ
Day 0:
Infect R.O.
Listeria Monocytogenes-GP33
Day 31:
Assess donor cells
in spleen
B
GP33+
Cells per spleen (10⁴)
C
CD127- KLRG1+
D
CD127+ KLRG1-
E
CD27- CD43-
F
CD27+ CD43+
% of GP33+
Cells per spleen (10³)
G
WT-P14
Day -1:
Transfer
WT - CD45.1
Malat1scr/scr - P14
Day 0:
Infect R.O.
Listeria Monocytogenes-GP33
Day 7:
Assess donor cells
in liver & spleen
Day 31:
Assess donor cells
in liver & spleen
H
Day 7 P14
Day 31 P14
spleen
liver
cells per spleen (10⁴)
cells per g liver (10⁴)
Day 7
L
WT
Malat1scr/scr
Liver
Spleen
KLRG1
CD127
9%
23%
8%
60%
10%
28%
9%
53%
12%
16%
12%
61%
20%
19%
20%
41%
I
CD127- KLRG1+
J
CD43- CD27-
K
CD43+ CD27+
% of P14
% of Parent
cells per spleen (10⁴)
cells per g liver (10⁴)
Day 31
M
WT
Malat1scr/scr
Liver
Spleen
CD27
CD43
35%
24%
39%
2%
32%
15%
51%
2%
39%
24%
33%
5%
29%
19%
46%
6%
N
KLRG1+
O
CD127+ KLRG1-
P
CD43- CD27-
Q
CD43+ CD27+
% of P14
% of Parent
cells per spleen (10³)
cells per g liver (10³)

Malat1 Enhances Cytotoxic T Cell IL-2 Production and Survival

Finally, we investigated how the Malat1:miR-15/16 RNA circuit regulates memory cell differentiation and accumulation, giving consideration to the many direct targets of miR-15/16 and the emergent indirect effects on IL-2 and other costimulation-responsive gene expression in CD8 T cells. The pro-survival protein Bcl2 is the first characterized target of miR-15/16 (Cimmino et al., 2005). Higher abundance of Bcl2 in memory cells (as compared with short-lived effector cells) aids their survival and persistence, counteracting their increased expression of pro-apoptotic factors such as Bim (Kurtulus et al., 2011). As such, changes in the balance of pro- and anti-apoptotic factors can have selective effects on the accumulation of memory T cells. Bcl2 expression in *Malat1*$^{scr/scr}$ P14 cells was reduced at day 31 in the CD43^{-} CD27^{-} population in both LCMV and LM-GP33 infection, and also in CD43^{+} CD27^{+} cells in LCMV infection (Fig 7A-C). This reduction is consistent with increased direct miR-15/16 action on the Bcl2 3' UTR in the *Malat1*$^{scr/scr}$ cells, but it may also be affected by IL-2 and other co-stimulation responsive factors. Also consistent with reduced Bcl2 expression, increased proportions of dead *Malat1*$^{scr/scr}$ cells were observed in both the KLRG1^{+} and KLRG1^{-} cell fractions at day 7 during LM-GP33 infection (Fig 7 D,E). Very few dead cells were detected among P14 cells of either genotype at day 31.

IL-2 is critical for the induction of Bcl2 in memory T cells to promote their survival (Toumi et al., 2022). Furthermore, IL-2 production by cytotoxic T cells predisposes them to differentiate into a memory phenotype, likely by an autocrine/paracrine mechanism (Kahan et al., 2022; Kurtulus et al., 2011; Wojciechowski et al., 2007). Given the enhanced ability of miR-15/16$^{\Delta/\Delta}$ cells to produce IL-2 and the trend toward impaired IL-2 production in *Malat1*$^{scr/scr}$ cells in vitro (Fig. 4D), we assessed IL-2 production by *Malat1*$^{scr/scr}$ T cells in LCMV and LM-GP33-infected mice. Corroborating our in vitro observations, a lower proportion of *Malat1*$^{scr/scr}$ P14 cells produced IL-2 when stimulated ex vivo on day 7 in both infection models (Fig 7F,G). This defect was also shared by KLRG1^{+} and KLRG1^{-} populations and limited to this critical early time point. Higher proportions of memory cells were able to produce IL-2 ex vivo at day 31 after infection with either LCMV or LM-GP33 infection, and *Malat1*$^{scr/scr}$ P14 cells produced equivalent amounts of IL-2 (Fig 7H).

As CD28 co-stimulation is key to IL-2 production, the observed early defect is consistent with less robust activation while antigen is still present (Shapiro et al., 1997-7). Taken together, these results indicate that *Malat1*$^{scr/scr}$ cells in the context of a viral or bacterial infection receive relatively poor activating cues and subsequently produce less IL-2 early during infection, contributing to a less robust pro-survival and pro-memory state. These findings illustrate how Malat1 regulation of miR-15/16 and its large target gene network can act through multiple connected nodes to coordinate gene expression programs essential to cytotoxic T cell responses.

Figure 7. Malat1 Enhances Pro-survival Cues Downstream of T cell activation

Malat1$^{scr/scr}$ and WT cells containing the GP33 specific TCR transgene (P14) on the CD45.2 background were transferred separately into congenic CD45.1 WT hosts. One day later the recipient mice were infected with $2*10^5$ p.f.u. I.p. lcmv armstrong or $2*10^4$ c.f.u. r.o. LM-GP33. Antigen specific responses were assayed by monitoring the transferred cells by flow cytometry in the spleen.

(A-C) Bcl2 expression in transferred P14 cells in the spleen 7 and 31 days post infection for both LCMV and LM-GP33. Data from two independent experiments per LCMV time point and a single experiment per LM-GP33 time point.

(A) Representative flow cytometry plots of P14 KLRG1$^+$ CD127$^-$ cell Bcl2 expression 7 days post infection. Numbers shown are mean fluorescence intensity.

(B) Representative flow cytometry plots of P14 CD43$^-$ CD27$^-$ cell Bcl2 expression 31 days post infection. Numbers shown are mean fluorescence intensity.

(C) Quantification of Bcl2 expression producing cells by mean fluorescence intensity within the indicated P14 subpopulation defined by KLRG1 or CD27 and CD43.

(D-E) Analysis of dead cells within splenic P14 CD43 and CD27 subpopulations at days 7 and 31 post LM-GP33 infection, data from a single experiment per time point.

(D) Representative flow cytometry plots of P14 subsets defined by CD43 and CD27. Numbers shown represent percent of dead cells per the parent subpopulation

(E) Quantification of dead cells as a percentage of parent P14 subpopulation

(F-G) Analysis of IL-2 producing P14 subsets in the spleen via IL-2 capture assay at days 7 and 31 post infection for both LCMV and LM-GP33, data from a single experiment per infection per time point.

(F) Representative flow cytometry plots of all P14 cells stained for KLRG1 and captured IL-2 from both infections at day 7. Numbers represent percent of cells in that quadrant of all P14 transferred cells.

(G) Quantification of IL-2 producing cells by percent of parent within the indicated P14 subpopulation defined by KLRG1 or CD27 and CD43.

Statistics displayed determined by unpaired t-test between *Malat1*$^{scr/scr}$ and WT transferred cells, where multiple tests were performed the Holm–Šidák method was used to correct for multiple comparisons (*, $p<0.05$; **, $p<0.01$)

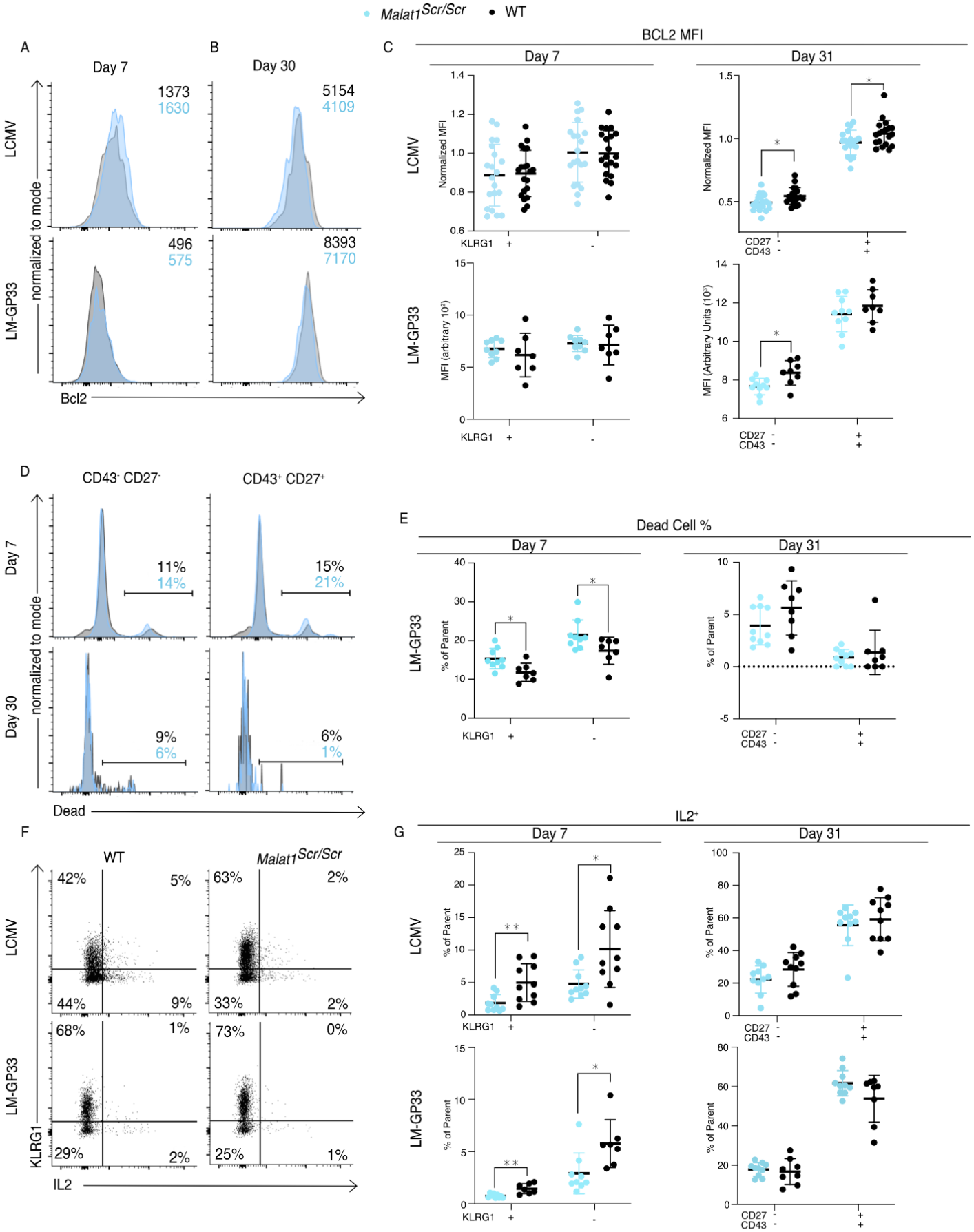
Malat1Scr/Scr
WT
A
Day 7
B
Day 30
LCMV
LM-GP33
normalized to mode
1373
1630
5154
4109
496
575
8393
7170
Bcl2
C
BCL2 MFI
Day 7
Day 31
Normalized MFI
MFI (arbitrary 10²)
MFI (Arbitrary Units (10³)
KLRG1
CD27
CD43
D
CD43⁻ CD27⁻
CD43⁺ CD27⁺
11%
14%
15%
21%
9%
6%
6%
1%
Dead
E
Dead Cell %
% of Parent
F
WT
42%
5%
44%
9%
63%
2%
33%
2%
68%
1%
29%
2%
73%
0%
25%
1%
KLRG1
IL2
G
IL2⁺

Discussion

LncRNAs are a large, diverse class of gene products that perform important physiological functions through a variety of molecular mechanisms. However, functional requirements are typically tested using RNAi to degrade the lncRNA or by disrupting their transcription entirely with no paradigm to dissect sequence specific functions. “Sponging” miRNAs (acting as a ceRNA) is among the most frequently proposed mechanisms of lncRNA function. Networks of noncoding ceRNAs, miRNAs, and target genes likely do shape gene expression programs in many biological contexts. Yet definitive evidence that a lncRNA:miRNA interaction has a physiological effect in a living organism has remained elusive. Guided by a biochemical approach, we investigated the requirements for Malat1 interaction with miR-15/16 by surgically altering just 5 nucleotides within the endogenous 8 kb Malat1 transcript in mice. Using T cells from these animals, we rigorously attribute changes in costimulation-responsive gene expression and in vivo defects in memory T cell formation to this Malat:miR-15/16 circuit.

Malat1 is a pleiotropic lncRNA implicated in a multitude of processes, including scaffolding splicing and epigenetic regulators, binding to chromatin, and interacting with several miRNAs in different cell types (Arun et al., 2020). Its extremely high expression and interspecies conservation nominated Malat1 as a strong candidate to have an impact on the activity of even highly abundant miRNAs like miR-15/16 that have large effects on gene expression and cell behavior. Less abundant miRNAs can also serve essential functions (Wigton et al., 2021), and they are likely to be more susceptible to inhibition by Malat1 and other ceRNAs. The same biochemically-driven sequence-specific approach used here could be applied to probe the physiological effects of other lncRNA:miRNA interactions, and it could also be extended to probe the requirement for interaction with Ezh2 and other proteins.

Another important future direction is to better understand how exactly Malat1 inhibits miR-15/16, given that TDMD does not appear to result from this interaction. Most Malat1 resides in the nucleus, whereas miRNAs reside and function in the cytoplasm. Advances in miRNA fluorescent in situ hybridization (miR-FISH) or the implementation of proximity-CLIP (Benhalevy et al., 2018) may help clarify whether Malat1 nuclear sequestration plays a role in its ceRNA function. Detailed mechanistic understanding of this experimentally tractable circuit may illuminate how ceRNAs may be leveraged by the cell or by cellular engineers to manipulate the miRNA pool and target gene expression.

There is a growing interest in Malat1 function within the immune system, where it is highly expressed in many cell types and often regulated in interesting ways, including differential expression in short lived effector and memory precursor cells produced by asymmetric division of activated T cells during LCMV infection (Kakaradov et al., 2017). Malat1 overexpression in dendritic cells promotes IL-10 production by T regulatory cells (Wu et al., 2018), and *Malat1*$^{-/-}$ mice exhibited reduced IL-10 and Maf expression by T helper cells in vivo and in vitro (Hewitson et al., 2020). Two prior reports addressed Malat1 function in cytotoxic T cell responses. In one report, no significant differences were observed in *Malat1*$^{-/-}$ mice (Yao et al., 2018). It is difficult to interpret negative data generated from whole-body Malat1 deficiency given the multitude of cell types in which Malat1 may act. A second recent report, using RNAi to suppress Malat1 expression specifically in antigen-specific CD8^{+} T cells, detected enhanced t-Tem differentiation (Kanbar et al., 2022). This observation, which contrasts with our findings using *Malat1*$^{scr/scr}$ mice, was suggested to occur via an epigenetic mechanism involving Malat1 interaction with Ezh2. This mechanism and the ceRNA function that we describe here are not mutually exclusive, and it is possible to observe divergent phenotypes from the different interventions used to probe Malat1 function in T cells.

Our *Malat1*$^{scr/scr}$ mouse combined with the cell transfer system clearly demonstrates a cytotoxic T cell intrinsic requirement for Malat1 to inhibit miR-15/16 to enhance activation and protect memory cell persistence. This is consistent with our previous work on the miR-15/16 family, and fitting with the increased expression of Malat1 in memory precursors (Gagnon et al., 2019; Kakaradov et al., 2017). The present study builds upon these findings and provides detailed insight into the gene regulatory programs which may drive these

phenotypes. Cytotoxic T cells lacking CD28 generate similar numbers of viral specific cells at the height of infection, but fail to maintain equivalent numbers during the memory phase (Borowski et al., 2007). Further, a major outcome of CD28 ligation is the production of IL-2, an essential T cell growth factor, and this IL-2 production is required in a cell intrinsic manner for generation of $CD127^+$ memory cells (Kahan et al., 2022). Here we demonstrate that not only does the Malat1-miR-15/16 circuit regulate CD28 co-stimulation, IL-2 production, and Bcl2 expression, but also the concordant outcome of maintaining $CD43^+$ $CD27^+$ memory cells. miR-15/16 targets a large number of genes, so it is unlikely that the effect on Bcl2 or CD28 alone is entirely responsible for the observed changes in $CD43^-$ $CD27^-$ t-TEM and $CD43^+$ $CD27^+$ memory cells. Our results are consistent with memory cells requiring a heightened level of pro-survival cues to survive the contraction bottleneck after the peak of infection. In this manner elevated Malat1 levels can act as an enhancer of pro-survival and activating cues to prevent excessive cell death in this sensitive memory population. The magnitude of this effect was modest in acute LCMV and Listeria infection, two models that feature robust pathogen clearance, allowing assessment of memory T cells in the absence of chronic antigen persistence. Further work is needed to probe other settings in which Malat1:miR-15/16 interaction may have a bigger impact on the outcome of immune responses.

The importance of cytotoxic T cells is evident in the context of the global COVID-19 pandemic and the advent of CAR-T cell therapies reaching the clinic. Knowledge of the networks that regulate these cells and the critical nodes within these networks have the potential to augment technologies and therapies from vaccines to anti-tumor immunotherapy. Transcription factors and miRNAs have been extensively studied in this fashion as critical nodes in the regulation of gene transcription and translation. In the study presented here, we show Malat1 acts upstream of one such node, the miR-15/16 family. From this one interaction, Malat1 has the potential to combinatorially and synergistically regulate gene networks essential to cytotoxic T cells. This concept is easily extended when Malat1's ability to regulate multiple other miRNA families is considered. If Malat1's sequence specific function is further defined, then editing or expression of specific Malat1 sequences could be used to tune multiple miRNA families in concert while leaving other functions of this enigmatic transcript un-touched.

Acknowledgements

We thank Shomyseh Sanjabi, Nadia Roan, and Jason Neidleman for generous donation of the LCMV armstrong virus; Michael Waterfield for generous donation of P14 mice; Marlys Fasset, Simon Zhou, and Eric Wigton for maintaining mutant mouse colonies through the COVID-19 pandemic; Walter Eckelbar, Eunice Wan, Charina Julian, Lenka Maliskova, and Andrew Schroeder for assistance with mRNA-seq and the sequencing of our HITS-CLIP libraries. This work was supported by the NIH (HL109102, HL107202), the Sandler Asthma Basic Research Center, and the Hooper Foundation. Priscila Muñoz-Sandoval is a Howard Hughes Medical Institute Gilliam Fellow. We acknowledge the PFCC (RRID:*SCR_018206*) for assistance generating Flow Cytometry data. Research reported here was supported in part by the DRC Center Grant NIH P30 DK063720.

Conflict of Interest

A.M. is a cofounder of Arsenal Biosciences, Spotlight Therapeutics, and Survey Genomics, serves on the boards of directors at Spotlight Therapeutics and Survey Genomics, is a board observer (and former member of the board of directors) at Arsenal Biosciences, is a member of the scientific advisory boards of Arsenal Biosciences, Spotlight Therapeutics, Survey Genomics, NewLimit, Amgen and Tenaya, owns stock in Arsenal Biosciences, Spotlight Therapeutics, NewLimit, Survey Genomics, PACT Pharma, and Tenaya and has received fees from Arsenal Biosciences, Spotlight Therapeutics, NewLimit, 23andMe, PACT Pharma, Juno Therapeutics, Trizell, Vertex, Merck, Amgen, Genentech, AlphaSights, Rupert Case Management, Bernstein and ALDA. A.M. is an investor in and informal advisor to Offline Ventures and a client of EPIQ. The Marson laboratory has received research support from Juno Therapeutics, Epinomics, Sanofi, GlaxoSmithKline, Gilead and Anthem. M.H.S. is founder and a board member of Teiko.bio and has received a speaking honorarium from Fluidigm Inc., has served as a consultant for Five Prime, Ono, January, Earli, Astellas, and Indaptus, and has received research funding from Roche/Genentech, Bristol Myers Squibb, Valitor, and Pfizer. J.D.G. is now an employee of Arsenal Biosciences.

Materials and Methods

Mice

WT C57/BL6 mice were bred in our facility. miR-15/16$^{\Delta/\Delta}$ and miR-15/16$^{fl/fl}$ mice were derived as described in Gagnon et al 2019. *Malat1*$^{scr/scr}$ mice were generated from WT C57/BL6 mouse zygotes electroportated with CRISPR-Cas9 RNPs and HDR template (guide and template sequences below) as described previously (Chen et al., 2016). B6.SJL-Ptprca Pepcb/BoyJ (CD45.1) strain #002014 were purchased from the Jackson Laboratory. WT P14 mice carrying the TCR transgene specific to the LCMV GP33 peptide were obtained from the Waterfield lab and were backcrossed to C57/BL6 to maintain the line. *Malat1*$^{scr/scr}$ mice were bred to the P14 line to generate *Malat1*$^{scr/scr}$ P14 mice. Male and female age and sex matched mice were used between 5 to 12 weeks of age. All mice were housed and bred in specific pathogen-free conditions in the Animal Barrier Facility at the University of California, San Francisco. Animal experiments were approved by the Institutional Animal Care and Use Committee of the University of California, San Francisco.

AGO2 HITS-CLIP

CD8+ T cells were isolated as below and stimulated for 3 days with αCD3 and αCD28 antibodies and grown with kool aid complete media. Subsequently the cells were rested and expanded in kool aid complete media for 2 days supplemented with 100 U/mL recombinant Human IL-2 (R&D Systems Cat# 202-IL-010/CF). Subsequently, $1*10^6$ cells were used to prepare NGS libraries as described in (Gagnon et al., 2019) & (Loeb et al., 2012). Samples were sequenced on HI-Seq 2500 (Illumina). 11 nucleotide adaptors were trimmed from each read and resultant sequences were aligned to the mm10 genome using bowtie2 (Langmead and Salzberg, 2012). To assure lack of miR-15/16 binding in *Malat1*$^{scr/scr}$ mice was not do to errors in alignment, reads from *Malat1*$^{scr/scr}$ cells were aligned to a mm10 genome that contained a single modification changing Malat1 from the WT allele to the *Malat1*^{scr} allele. To determine maximum binding depth across the genome and to manipulate aligned files the samtools package was used (Li et al., 2009). To assess Ago2 binding, aligned HITS-CLIP reads were integrated across the follow genomic annotations: lncRNA genes from mouse Noncode v6 (http://www.noncode.org/download.php); miRNA target binding sites from TargetScan V7.2 (https://www.targetscan.org/cgi-bin/targetscan/data_download.mmu80.cgi); mm10 introns, exons, 3'UTRs, and coding genes from UCSC genome table browser (http://genome.ucsc.edu/cgi-bin/hgGateway?db=mm10). To assess differences in target binding at specific 3' UTR sites between WT and *Malat1*$^{scr/scr}$ cells, reads within each 3' UTR were normalized to the total reads contained in the given 3' UTR for each genotype. To identify regions of significant Ago2 binding above background, so-called "peaks", we used the Piranha algorithm (https://github.com/smithlabcode/piranha) on our HITS-CLIP. To remove sites from analysis where confounding features were present, such as miRNA expression sites or rRNA repeats, bedtools intersect was used to remove these features from annotation files (Quinlan, 2014). Human AHC data from publicly available datasets were trimmed and aligned to the Hg38 genome as previously described (Karginov and Hannon, 2013; Li et al., 2018).

Cell Transfer and Infections

Spleens were harvested from WT or *Malat1*$^{scr/scr}$ P14 CD45.2 mice into PBS and passed through 70 µm strainers to generate a single cell suspension. Samples were then stained for live/dead (apc-cy7), Thy1.2 (BV605), CD8α (apc), and TCRVα2 (pe). Whole splenocytes were then transferred retro-orbitally (r.o.) into WT BoyJ (CD45.1) 7 week old male recipients such that each recipient received 20,000 Thy1.2$^+$ CD8α$^+$ TCRVα2$^+$ cells in 200 µL PBS. To initiate LCMV infections, mice were injected intraperitoneally (i.p.) with $2*10^5$ plaque forming units (p.f.u.) LCMV armstrong in 200 uL plain RPMI. LCMV virus was produced in house as described in (Shehata et al., 2018). To initiate *Listeria Monocytogenes* infection, mice were injected r.o. with $2*10^5$ colony forming units (c.f.u.) *Listeria Monocytogenes-GP33* in 100 uL PBS. *Listeria Monocytogenes-GP33* was prepared in house as described in (Allen et al., 2020). Blood was collected via submandibular bleeds with goldenrod 4 mm lancets collected into sample tubes coated with K2 EDTA (BD Ref# 365974) and 60 µL of blood was lysed with 500 uL of ACK lysis buffer. To assay spleens and livers, mice were sacrificed and organs harvested. To assay intracellular cytokine production, splenocytes were plated into 96-well u-bottom plates in complete kool-AID media and stimulated for 6 hours with a final concentration of 0.2 mg/ml GP33-41 (KAVYNFATM) in the presence of Brefeldin A.

Flow Cytometry

Spleens and livers were harvested into 2% FBS PBS with and passed through 70 µm strainers to generate a single cell suspension. Samples were then spun at 450 r.c.f. for 5 minutes and livers were resuspended in 20% Percoll. Percoll suspensions were spun at 741 r.c.f for 20 minutes at 25°C and the supernatants discarded. Cell pellets for both spleens and livers were resuspended in 1 mL ACK lysis buffer and incubated at 4°C for 5

minutes. Lysis was stopped with 5 mL 2% FBS PBS and samples again spun at 450 r.c.f. for 5 minutes. Samples were resuspended in 2% FCS PBS and aliquoted into v-bottom 96 well plates. Live dead staining was then performed using the fixable viability dye at 1:2000 in PBS. Subsequently, cells were blocked with mouse Fc block 1:100 in 2% FCS PBS and stained for surface proteins with directly conjugated antibodies diluted 1:100 in 2% FCS PBS. Stains were incubated for 20 minutes at 4°C protected from light. For surface stains alone, LCMV samples were fixed with 4% PFA for 5 minutes at 4°C. For intracellular stains, samples were fixed and permeabilized according the the Transcription Factor FIxation Kit (Invitrogen Cat#00-5521-00). Intracellular antibodies were diluted in 1:100 in permeabilization buffer and incubated at 4°C for 30 minutes. All samples were spun at 821 r.c.f. for 5 minutes prior to being resuspended in 2% FCS PBS with 1:10 AccuCount beads (spherotech Cat #ACBP-100-10) for analysis on either the BD LSR II or the BD LSRFortessa flow cytometry analyzer.

Cell Isolation and In Vitro Functional Assays

CD8+ T cells were isolated from spleens using negative selection from the EasySep Mouse CD8+ T Cell Isolation Kit (cat# 19853). Cells were counted using trypan blue staining and the nexelcom cellometer spectrum. Cultures were started via stimulation with plate bound αCD3 (1 µg/mL, clone 2C11) and αCD28 (1 µg/mL, clone 37.51); plates coated overnight in PBS with Ca++ & Mg++ at 4°C. Cells were plated in Kool AID complete media (DMEM high glucose media supplemented with 10% FCS, pyruvate, nonessential amino acids, MEM vitamins, L-arginine, L-asparagine, L-glutamine, folic acid, beta mercaptoethanol, penicillin, and streptomycin) and spun at 450 r.c.f. for 5 minutes at 25°C to begin stimulation. For functional assays cells were harvested 2 or 4 hours after stimulation for flow cytometry, or 24 hours after stimulation for mRNA-seq. For supernatant cytokine expression, plates were spun at 450 r.c.f. for 5 minutes at 4°C 16 hours after stimulation and cell free culture medium was collected and frozen at -80°C. TNFα (Cat #), IFNɣ (Cat #), and IL-2 (Cat #) were analyzed by ELISA.

miRNA qPCR

Spleens were harvested and single cell suspensions generated by passing through 70µm strainers. CD8+ T cells were isolated as above, and $2*10^6$ cells were pelleted at 450 r.c.f. for 5 minutes at 4°C. Cell pellet was resuspended in 700 uL Trizol reagent (Ambion cat #15596018) and kept at -80°C. RNA was was isolated using using the Direct-zol-96 RNA Kit (zymogen Cat #R2054). This RNA was used as input to the Mir-X™ miRNA qRT-PCR TB Green® Kit (Takara cat# 638316) to generate miRNA cDNA. Specific primers to miR-15a, miR-15b, and miR-16 were used to quantify those miRNA species on the QPCR MACHINE (eppendorf realplex[2]). ribosomalRNA 5.8s was used as a housekeeping control for each sample. Each sample was run in duplicate. To quantify miRNA expression technical duplicates were averaged and then normalized to rRNA 5.8s by subtracting the rRNA 5.8s Ct value from miRNA Ct value (ΔCt). Expression values reported are generated by $2^{-\Delta Ct}$.

mRNA Sequencing

$1*10^6$ CD8+ T cells were harvested 24 hours after αCD3 ± αCD28 stimulation as described above. Cells were pelleted at 450 r.c.f. for 5 minutes at 4°C. Cell pellet was resuspended in 700 uL Trizol reagent (ambion ref #15596018) and kept at -80°C. RNA was was isolated using using the Direct-zol-96 RNA Kit (zymogen Cat #R2054). The integrity of total RNA was checked on Fragment Analyzer (Agilent, Cat. No. DNF-472), only RNA with RQN number of above 7 was used for library construction. The starting quantity of 100ng of total RNA was used according to vendor instructions with Universal plus mRNA with Nu Quant (TECAN, Cat. No. 0520), final library PCR amplification was 17 cycles. After library completion, individual libraries were pooled equally by

volume, and quantified on Fragment Analyzer (Agilent, Cat. No. DNF-474). Quantified library pool was diluted to 1nM and further diluted as per protocol and sequenced on Illumina MiniSeq (Illumina, Cat. No. FC-420-1001) to check for quality of reads. Finally, individual libraries were normalized according to MiniSeq output reads, specifically by % protein coding genes and were sequenced on one lane of NovaSeq6000 S4 PE100 (Illumina, Cat. No. 20028313). Reads were aligned to the mouse genome GRCm38 and quantified using the STAR aligner software version 2.7.2b. Read normalization and differential expression analysis was performed in the R computing environment version 3.6.1 using the software DESeq2 version 1.26. For RNA sequencing analysis, FDR-corrected p-values were used to evaluate significant differences between experimental groups using a significance threshold of 0.05. Lowly expressed genes that had fewer than 2 reads per million on average across all samples were removed from the analysis. Empirical cumulative density plots were made using the ggplot package for R. Heatmaps and hierarchical clustering was performed via the gplots package for R. Gene ontology analysis was performed using the statistical overrepresentation test for Panther pathways (Mi et al., 2019).

Statistical and Analytical Software

All flow cytometry data was analyzed using FlowJo (version 10). Statistical analyses and plotting was performed using Graphpad Prism (Version 9.2.0) and R (version 4.2.1).

Data Availability and Software

Ago2 HITS-CLIP data uploaded to NCBI GEO accession #GSE216565.
mRNA sequencing data uploaded to NCBI GEO accession #GSE216113.
Code used to analyze HITS-CLIP data summed over annotations and peaks in WT cells can be found at github.com/AnselLab/WT_HITS_CLIP_Analyses.
Code used to analyze relative binding densities of HITS-CLIP reads can be found at github.com/AnselLab/Malat1_miR1516_AGO2_HITS_CLIP.
Code used to analyze mRNAseq data for both miR-15/16 target expression and CD28 responsive genes can be found at github.com/AnselLab/Malat1_miR1516_CD3CD28_RNAseq.

Key Reagent Table

Reagent	Source	Detail	Catalog #
IL-2 ELISA	Invitrogen		5018280
TNFα ELISA	Invitrogen		BMS607-3
IFNɣ ELISA	R&D Systems		MIF00
IL-2 Secretion Assay APC	Miltenyi Biotec		130-090-987

Malat1 CRISPR Guide 1	Dharmacon	Sequence - GCATTCTAATAGCAGCAGAT	
Malat1 HDRT Ultramer	IDT	Sequence - ACAGACCACACAGAATGCAGGTGTCTTGACTTCAGGTCATGTCTGTTCTTTGGCAAGTAATATGTGCAGTACTGTTCCAATCTGTCCTGATTAGAATGCATTGTGACGCGACTGGAGTATGATTAAAGAAAGTTGTGTTTCCCCAAGTGTTTGGAGTAGTGGTTGTTGGAGGAAAAGCCATGAGTAACAGGCTGAGTGTT	
anti-CD127 PE	invitrogen	Clone-A7R34	12-1271-83
anti-CD127 FITC	invitrogen	Clone-A7R34	11-1271-82
anti-CD45.2 BV785	BioLegend	Clone-104	109839
anti- CD45.1 Alexa Fluor 700	BioLegend	Clone-A20	110724
anti-CD90.2 BV605	BD Biosciences	Clone-30-H12	740334
anti-CD90.2 eFluor 450	eBiosciences	Clone-53-2.1	48-0902-80
anti-CD44 PE-Cy7	eBiosciences	Clone-IM7	25-0441-82
anti-CD27 APC	eBiosciences	Clone-LG.7F9	17-0271-82
anti-CD27 FITC	eBiosciences	Clone-LG.7F9	11-0271-82
anti-Bim PE	Cell Signaling	Clone-C34C5	12186S
anti-CD43 Percp-Cy5.5	BioLegend	Clone-1B11	121224
anti-CD45.2 PE-Cy7	BD Biosciences	Clone-104	560696
anti-CD45.1 BV785	BioLegend	Clone-A20	110743
anti-Bcl2 Alexa Fluor 647	BioLegend	Clone-BCL/10C4	633510
anti-Bim Alexa Fluor 700	Cell Signaling	Clone-C34C5	28997S
GP33 Tetramer PE	NIH Tetramer Core	Peptide: KAVYNFATM	57624
anti-KLRG1 BV711	BD Bioscience	Clone-2F1	564014
Fixable Viability Dye eFluor 780	eBioscience		65-0865-14

anti-CD8α BV805	BD Bioscience	Clone-53-6.7	612898
anti-CD28 FITC	BioLegend	Clone-E18	122008
anti-CD69 APC	Invitrogen	Clone-H1.2F3	17-0691-82
anti-Nur77 PE	Invitrogen	Clone-12.14	12-5965-80
anti-CD62L BV605	BD Biosciences	Clone-MEL-14	563252

Supplemental Data & Figures

Figure S1. *Malat1*^{scr} allele does not disrupt other miRNA families

TargetScan predicted binding sites for highly expressed microRNA families in T cells that contained at least one HITS-CLIP read in both WT and Malat1$^{scr/scr}$ CD8^{+} T cells were compared for depth of Ago2 HITS-CLIP reads. First, reads at the predicted seed site were normalized by total Ago2 HITS-CLIP reads in a given 3' UTR. To best visualize all sites, logit transforms of these values are plotted. Paired t-test performed to determine significance. Blue line indicates the identity line. Data for each genotype is from combined libraries of n = 2 biological replicates.

(A) Predicted sites for let-7-5p
(B) Predicted sites for miR-21-5p
(C) Predicted sites for miR-101-3p
(D) Predicted sites for miR-142-3p

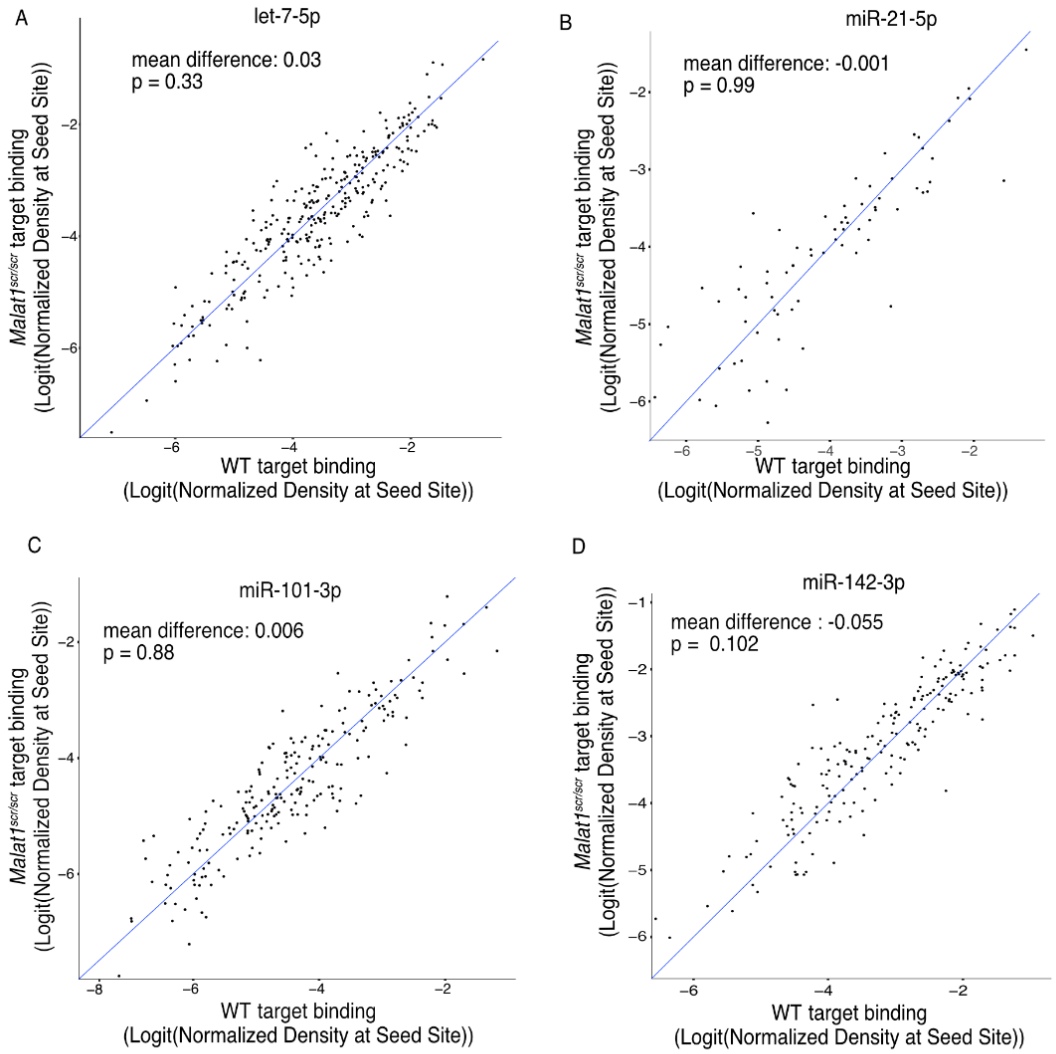
A
let-7-5p
mean difference: 0.03
p = 0.33
Malat1scr/scr target binding
(Logit(Normalized Density at Seed Site))
WT target binding
(Logit(Normalized Density at Seed Site))
B
miR-21-5p
mean difference: -0.001
p = 0.99
Malat1scr/scr target binding
(Logit(Normalized Density at Seed Site))
WT target binding
(Logit(Normalized Density at Seed Site))
C
miR-101-3p
mean difference: 0.006
p = 0.88
Malat1scr/scr target binding
(Logit(Normalized Density at Seed Site))
WT target binding
(Logit(Normalized Density at Seed Site))
D
miR-142-3p
mean difference : -0.055
p = 0.102
Malat1scr/scr target binding
(Logit(Normalized Density at Seed Site))
WT target binding
(Logit(Normalized Density at Seed Site))

Figure S2. AHC and gene expression analyses nominate direct miR-15/16 targets involved in growth signaling pathways

(A) Heat map indicating differential gene expression between WT and *Malat1*$^{scr/scr}$ cells, and between miR-15/16$^{fl/fl}$ cells and miR-15/16$^{\Delta/\Delta}$ cells in RNA sequencing analyses.
(B-C) Histograms of AHC mapping of Ago2 binding in the 3' UTR of *Pik3r1* (B) and *Mapk8* (C) in WT (black), miR-15/16$^{\Delta/\Delta}$ (red) and *Malat1*$^{scr/scr}$ (blue) cells. As in Figure 3, AHC libraries were generated from CD8^{+} T cells isolated from spleens and cultured for 5 days (combined libraries from n = 2 for each genotype). Grey bars indicate the peaks containing TargetScan predicted miR-15/16 binding sites.

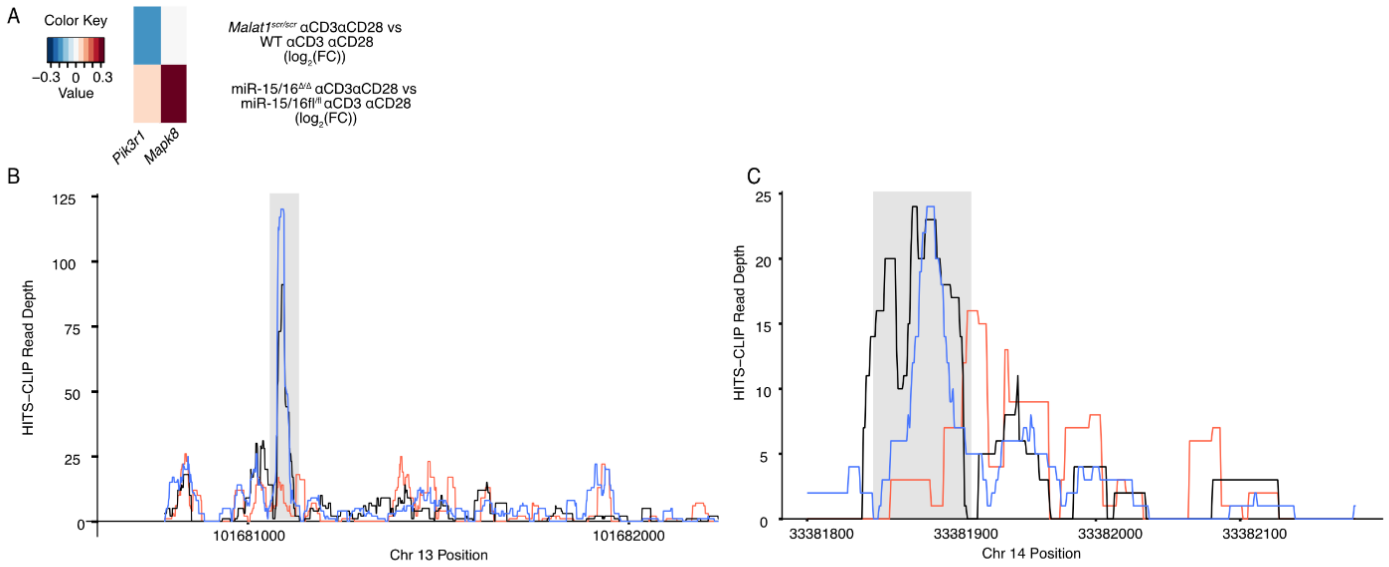

Figure S3. CD28 responsive genes are induced by αCD28 stimulation in all genotypes tested

Cumulative density plots comparing expression of CD28 responsive gene set defined as genes from (Martínez-Llordella et al., 2013) with αCD3αCD28 vs αCD3 $\log_2$(FC) > 1.5 and adjusted p value < 0.001. Kolmogorov-Smirnov test used to determine significant differences in the distributions of target and non-target genes. αCD3 used at 1 μg/mL, and α CD28 used at 1 μg/mL. Data are from a single experiment with n=6 for each genotype and stimulation condition combination.
(A) Comparison of CD28 responsive genes in WT cells
(B) Comparison of CD28 responsive genes in *Malat1*$^{scr/scr}$ cells
(C) Comparison of CD28 responsive genes in miR-15/16$^{fl/fl}$ cells
(D) Comparison of CD28 responsive genes in miR-15/16$^{\Delta/\Delta}$ cells

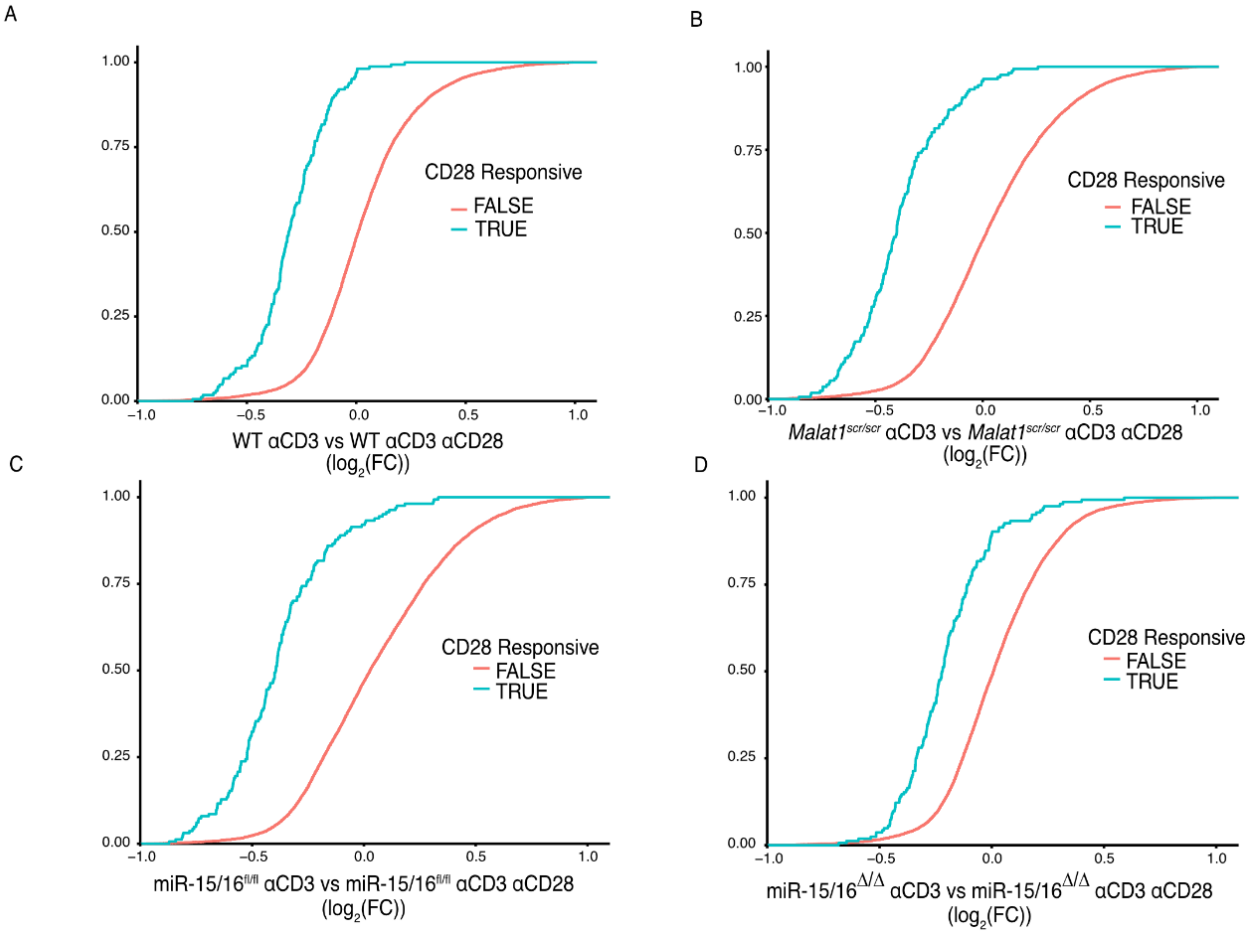
A
1.00
0.75
0.50
0.25
0.00
−1.0
−0.5
0.0
0.5
1.0
CD28 Responsive
FALSE
TRUE
WT αCD3 vs WT αCD3 αCD28
(log2(FC))
B
Malat1scr/scr αCD3 vs Malat1scr/scr αCD3 αCD28
(log2(FC))
C
miR-15/16fl/fl αCD3 vs miR-15/16fl/fl αCD3 αCD28
(log2(FC))
D
miR-15/16Δ/Δ αCD3 vs miR-15/16Δ/Δ αCD3 αCD28
(log2(FC))

Figure S4. Malat1 Regulates Memory Formation in Unchallenged Poly Clonal Animals

Cells were isolated from the spleens of young, age-matched, naive mice and analyzed by flow cytometry for CD44 and CD62L to delineate naive, effector memory, and central memory cells. Results shown are gated on $CD8^+$ $CD5^+$ lymphocytes. Data for *Malat1*$^{scr/scr}$ and WT cells are from 3 independent experiments. Data for miR-15/16$^{fl/fl}$ and miR-15/16$^{\Delta/\Delta}$ cells are from 2 independent experiments. Statistics displayed determined by unpaired t-test between Malat1$^{scr/scr}$ and WT cells or between miR-15/16$^{fl/fl}$ and miR-15/16$^{\Delta/\Delta}$ cells (*, $p<0.05$; **, $p<0.01$)

(A) Representative flow cytometry plots of CD44 and CD62L for each genotype assayed. Percentages shown are of CD8+ population.

(B) Quantification of naive cells ($CD62L^+$ $CD44^-$)

(C) Quantification of central memory cells ($CD62L^+$ $CD44^+$)

(D) Quantification of effector memory cells ($CD62L^-$ $CD44^+$)

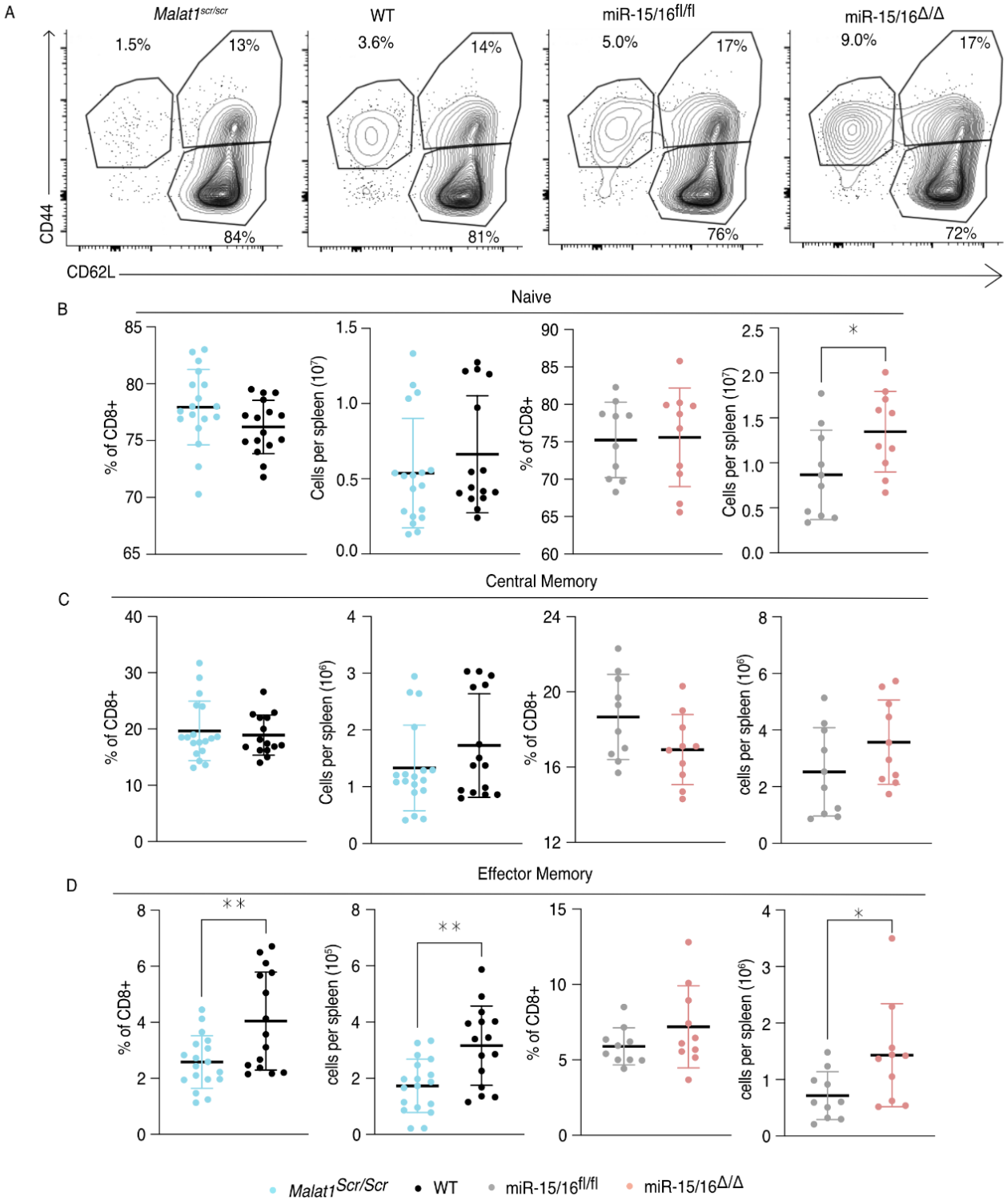
A
Malat1scr/scr
WT
miR-15/16fl/fl
miR-15/16Δ/Δ
1.5%
13%
84%
3.6%
14%
81%
5.0%
17%
76%
9.0%
17%
72%
CD44
CD62L
Naive
B
% of CD8+
Cells per spleen (10^7)
Central Memory
C
Cells per spleen (10^6)
cells per spleen (10^6)
Effector Memory
D
cells per spleen (10^5)
Malat1Scr/Scr
WT
miR-15/16fl/fl
miR-15/16Δ/Δ

Figure S5. Malat1 is epistatic to miR-15/16 in the regulation memory cell expansion following LCMV infection

Polyclonal mice of the miR-15/16$^{fl/fl}$, miR-15/16$^{\Delta/\Delta}$, and *Malat1*$^{scr/scr}$;miR-15/16$^{\Delta/\Delta}$ genotypes were directly infected i.p. with 5*10^5 p.f.u. I.p. lcmv armstrong. Antigen specific responses were tracked in the blood and spleen using the GP33 tetramer at day 7 and day 31 post infection.

(A) Representative flow cytometry plots illustrating the gating on antigen specific cells using CD44 and GP33

(B) Quantification of GP33+ cells in the blood at day 7

(C) Quantification of GP33+ cells in the spleen at day 31 by absolute numbers and percent of the CD8+ T cell population

(D) Representative flow cytometry plots of KLRG1 and CD127 expression at day 31 in the antigen specific cell population

(E) Representative flow cytometry plots of CD27 and CD43 expression at day 31 in the antigen specific cell population

(F) Quantification of KLRG1$^+$ antigen specific cells in the blood at day 7 by relative percentage and absolute numbers

(G) Quantification of KLRG1+ antigen specific cells in the spleen at day 31 by relative percentage and absolute numbers

(H) Quantification of CD43+ CD27+ memory cells in the spleen at day 31 by relative percentage and absolute numbers

(I) Quantification of CD43- CD27- t-Tem cells in the spleen at day 31 by relative percentage and absolute numbers

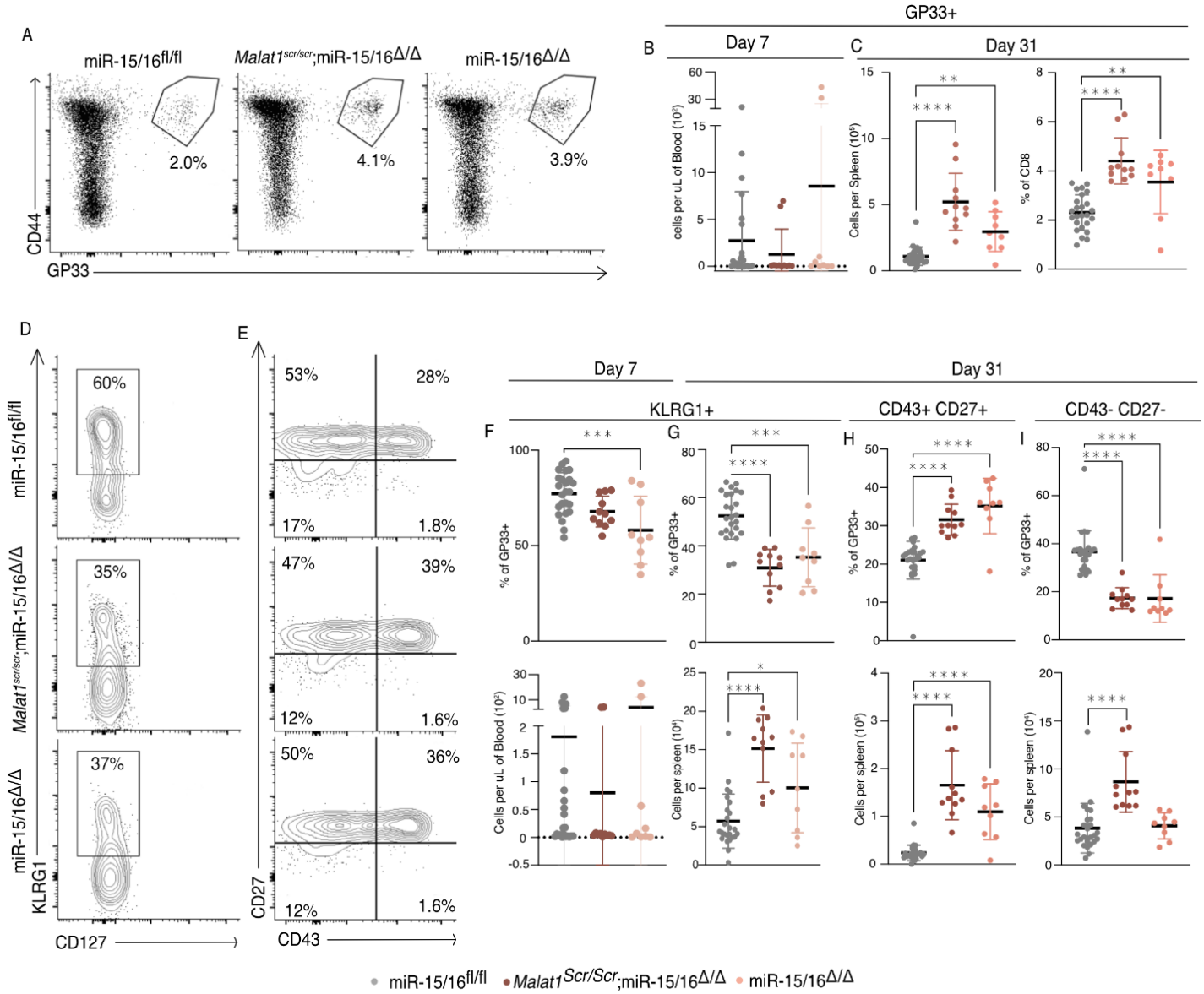
A
miR-15/16fl/fl
Malat1scr/scr;miR-15/16Δ/Δ
miR-15/16Δ/Δ
2.0%
4.1%
3.9%
CD44
GP33
GP33+
B
Day 7
C
Day 31
cells per uL of Blood (10³)
Cells per Spleen (10⁶)
% of CD8
D
E
60%
35%
37%
53%
28%
17%
1.8%
47%
39%
12%
1.6%
50%
36%
12%
1.6%
miR-15/16fl/fl
Malat1scr/scr;miR-15/16Δ/Δ
miR-15/16Δ/Δ
KLRG1
CD127
CD27
CD43
Day 7
Day 31
KLRG1+
CD43+ CD27+
CD43- CD27-
F
G
H
I
% of GP33+
Cells per uL of Blood (10³)
Cells per spleen (10⁶)
miR-15/16fl/fl
Malat1Scr/Scr;miR-15/16Δ/Δ
miR-15/16Δ/Δ

Allen BM, Hiam KJ, Burnett CE, Venida A, DeBarge R, Tenvooren I, Marquez DM, Cho NW, Carmi Y, Spitzer MH. 2020. Systemic dysfunction and plasticity of the immune macroenvironment in cancer models. *Nat Med* **26**:1125–1134.

Arun G, Aggarwal D, Spector DL. 2020. MALAT1 Long Non-Coding RNA: Functional Implications. *Noncoding RNA* **6**. doi:10.3390/ncrna6020022

Ashouri JF, Weiss A. 2017. Endogenous Nur77 Is a Specific Indicator of Antigen Receptor Signaling in Human T and B Cells. *J Immunol* **198**:657–668.

Bachmann MF, Barner M, Viola A, Kopf M. 1999. Distinct kinetics of cytokine production and cytolysis in effector and memory T cells after viral infection. *Eur J Immunol* **29**:291–299.

Badovinac VP, Porter BB, Harty JT. 2002. Programmed contraction of CD8(+) T cells after infection. *Nat Immunol* **3**:619–626.

Bartel DP. 2018. Metazoan MicroRNAs. *Cell* **173**:20–51.

Benhalevy D, Anastasakis DG, Hafner M. 2018. Proximity-CLIP provides a snapshot of protein-occupied RNA elements in subcellular compartments. *Nat Methods* **15**:1074–1082.

Blattman JN, Grayson JM, Wherry EJ, Kaech SM, Smith KA, Ahmed R. 2003. Therapeutic use of IL-2 to enhance antiviral T-cell responses in vivo. *Nat Med* **9**:540–547.

Borowski AB, Boesteanu AC, Mueller YM, Carafides C, Topham DJ, Altman JD, Jennings SR, Katsikis PD. 2007. Memory CD8+ T cells require CD28 costimulation. *J Immunol* **179**:6494–6503.

Carrieri C, Cimatti L, Biagioli M, Beugnet A, Zucchelli S, Fedele S, Pesce E, Ferrer I, Collavin L, Santoro C, Forrest ARR, Carninci P, Biffo S, Stupka E, Gustincich S. 2012. Long non-coding antisense RNA controls Uchl1 translation through an embedded SINEB2 repeat. *Nature* **491**:454–457.

Chen L, Yao H, Wang K, Liu X. 12 2017. Long Non-Coding RNA MALAT1 Regulates ZEB1 Expression by Sponging miR-143-3p and Promotes Hepatocellular Carcinoma Progression. *J Cell Biochem* **118**:4836–4843.

Chen S, Lee B, Lee AY-F, Modzelewski AJ, He L. 2016. Highly Efficient Mouse Genome Editing by CRISPR Ribonucleoprotein Electroporation of Zygotes. *J Biol Chem* **291**:14457–14467.

Chen Y, Zander R, Khatun A, Schauder DM, Cui W. 2018. Transcriptional and Epigenetic Regulation of Effector and Memory CD8 T Cell Differentiation. *Front Immunol* **9**:2826.

Cimmino A, Calin GA, Fabbri M, Iorio MV, Ferracin M, Shimizu M, Wojcik SE, Aqeilan RI, Zupo S, Dono M, Rassenti L, Alder H, Volinia S, Liu C-G, Kipps TJ, Negrini M, Croce CM. 2005. *miR-15* and *miR-16* induce apoptosis by targeting BCL2. *Proc Natl Acad Sci U S A* **102**:13944–13949.

Djuranovic S, Nahvi A, Green R. 2012. miRNA-mediated gene silencing by translational repression followed by mRNA deadenylation and decay. *Science* **336**:237–240.

Eberlein J, Davenport B, Nguyen TT, Victorino F, Sparwasser T, Homann D. 2012-2. Multiple Layers of CD80/86-Dependent Costimulatory Activity Regulate Primary, Memory, and Secondary Lymphocytic Choriomeningitis Virus-Specific T Cell Immunity. *J Virol* **86**:1955–1970.

Eichhorn SW, Guo H, McGeary SE, Rodriguez-Mias RA, Shin C, Baek D, Hsu S-H, Ghoshal K, Villén J, Bartel DP. 2014. mRNA destabilization is the dominant effect of mammalian microRNAs by the time substantial repression ensues. *Mol Cell* **56**:104–115.

Elguindy MM, Mendell JT. 2021. NORAD-induced Pumilio phase separation is required for genome stability. *Nature* **595**:303–308.

Faghihi MA, Modarresi F, Khalil AM, Wood DE, Sahagan BG, Morgan TE, Finch CE, St Laurent G 3rd, Kenny PJ, Wahlestedt C. 2008. Expression of a noncoding RNA is elevated in Alzheimer's disease and drives rapid feed-forward regulation of beta-secretase. *Nat Med* **14**:723–730.

Fraser JD, Irving BA, Crabtree GR, Weiss A. 1991. Regulation of interleukin-2 gene enhancer activity by the T cell accessory molecule CD28. *Science* **251**:313–316.

Fuse S, Zhang W, Usherwood EJ. 2008. Control of memory CD8+ T cell differentiation by CD80/CD86-CD28 costimulation and restoration by IL-2 during the recall response. *J Immunol* **180**:1148–1157.

Gagnon JD, Kageyama R, Shehata HM, Fassett MS, Mar DJ, Wigton EJ, Johansson K, Litterman AJ, Odorizzi P, Simeonov D, Laidlaw BJ, Panduro M, Patel S, Jeker LT, Feeney ME, McManus MT, Marson A, Matloubian M, Sanjabi S, Ansel KM. 2019. miR-15/16 Restrain Memory T Cell Differentiation, Cell Cycle, and Survival. *Cell Rep* **28**:2169–2181.e4.

Gong C, Maquat LE. 2011. lncRNAs transactivate STAU1-mediated mRNA decay by duplexing with 3' UTRs via Alu elements. *Nature* **470**:284–288.

Grujic M, Bartholdy C, Remy M, Pinschewer DD, Christensen JP, Thomsen AR. 2010. The role of CD80/CD86

in generation and maintenance of functional virus-specific CD8+ T cells in mice infected with lymphocytic choriomeningitis virus. *J Immunol* **185**:1730–1743.
Han J, LaVigne CA, Jones BT, Zhang H, Gillett F, Mendell JT. 2020. A ubiquitin ligase mediates target-directed microRNA decay independently of tailing and trimming. *Science* **370**. doi:10.1126/science.abc9546
Hewitson JP, West KA, James KR, Rani GF, Dey N, Romano A, Brown N, Teichmann SA, Kaye PM, Lagos D. 2020. Malat1 Suppresses Immunity to Infection through Promoting Expression of Maf and IL-10 in Th Cells. *The Journal of Immunology*. doi:10.4049/jimmunol.1900940
Hikono H, Kohlmeier JE, Takamura S, Wittmer ST, Roberts AD, Woodland DL. 2007. Activation phenotype, rather than central- or effector-memory phenotype, predicts the recall efficacy of memory CD8+ T cells. *J Exp Med* **204**:1625–1636.
Ji P, Diederichs S, Wang W, Böing S, Metzger R, Schneider PM, Tidow N, Brandt B, Buerger H, Bulk E, Thomas M, Berdel WE, Serve H, Müller-Tidow C. 2003. MALAT-1, a novel noncoding RNA, and thymosin beta4 predict metastasis and survival in early-stage non-small cell lung cancer. *Oncogene* **22**:8031–8041.
Kahan SM, Bakshi RK, Ingram JT, Hendrickson RC, Lefkowitz EJ, Crossman DK, Harrington LE, Weaver CT, Zajac AJ. 2022. Intrinsic IL-2 production by effector CD8 T cells affects IL-2 signaling and promotes fate decisions, stemness, and protection. *Sci Immunol* **7**:eabl6322.
Kakaradov B, Arsenio J, Widjaja CE, He Z, Aigner S, Metz PJ, Yu B, Wehrens EJ, Lopez J, Kim SH, Zuniga EI, Goldrath AW, Chang JT, Yeo GW. 2017. Early transcriptional and epigenetic regulation of CD8 + T cell differentiation revealed by single-cell RNA sequencing. *Nat Immunol* **18**:422–432.
Kanbar JN, Ma S, Kim ES, Kurd NS, Tsai MS, Tysl T, Widjaja CE, Limary AE, Yee B, He Z, Hao Y, Fu X-D, Yeo GW, Huang WJ, Chang JT. 2022. The long noncoding RNA Malat1 regulates CD8+ T cell differentiation by mediating epigenetic repression. *J Exp Med* **219**. doi:10.1084/jem.20211756
Karginov FV, Hannon GJ. 2013. Remodeling of Ago2-mRNA interactions upon cellular stress reflects miRNA complementarity and correlates with altered translation rates. *Genes Dev* **27**:1624–1632.
Kleaveland B, Shi CY, Stefano J, Bartel DP. 2018. A Network of Noncoding Regulatory RNAs Acts in the Mammalian Brain. *Cell* **174**:350–362.e17.
Kopp F, Mendell JT. 2018. Functional Classification and Experimental Dissection of Long Noncoding RNAs. *Cell* **172**:393–407.
Kurtulus S, Tripathi P, Moreno-Fernandez ME, Sholl A, Katz JD, Grimes HL, Hildeman DA. 2011. Bcl-2 allows effector and memory CD8+ T cells to tolerate higher expression of Bim. *J Immunol* **186**:5729–5737.
Langmead B, Salzberg SL. 2012. Fast gapped-read alignment with Bowtie 2. *Nat Methods* **9**:357–359.
Lee JT, Davidow LS, Warshawsky D. 1999. Tsix, a gene antisense to Xist at the X-inactivation centre. *Nat Genet* **21**:400–404.
Li H, Handsaker B, Wysoker A, Fennell T, Ruan J, Homer N, Marth G, Abecasis G, Durbin R, 1000 Genome Project Data Processing Subgroup. 2009. The Sequence Alignment/Map format and SAMtools. *Bioinformatics* **25**:2078–2079.
Liu Q, Fu H, Sun F, Zhang H, Tie Y, Zhu J, Xing R, Sun Z, Zheng X. 2008. miR-16 family induces cell cycle arrest by regulating multiple cell cycle genes. *Nucleic Acids Res* **36**:5391–5404.
Liu W, Wang X. 2019. Prediction of functional microRNA targets by integrative modeling of microRNA binding and target expression data. *Genome Biol* **20**:18.
Li Y, Estep JA, Karginov FV. 2018. Transcriptome-wide Identification and Validation of Interactions between the miRNA Machinery and HuR on mRNA Targets. *J Mol Biol* **430**:285–296.
Loeb GB, Khan AA, Canner D, Hiatt JB, Shendure J, Darnell RB, Leslie CS, Rudensky AY. 2012. Transcriptome-wide miR-155 binding map reveals widespread noncanonical microRNA targeting. *Mol Cell* **48**:760–770.
Luan W, Li L, Shi Y, Bu X, Xia Y, Wang J, Djangmah HS, Liu X, You Y, Xu B. 2016. Long non-coding RNA MALAT1 acts as a competing endogenous RNA to promote malignant melanoma growth and metastasis by sponging miR-22. *Oncotarget* **7**:63901–63912.
Maggirwar SB, Harhaj EW, Sun SC. 1997. Regulation of the interleukin-2 CD28-responsive element by NF-ATp and various NF-kappaB/Rel transcription factors. *Mol Cell Biol* **17**:2605–2614.
Martínez-Llordella M, Esensten JH, Bailey-Bucktrout SL, Lipsky RH, Marini A, Chen J, Mughal M, Mattson MP, Taub DD, Bluestone JA. 2013. CD28-inducible transcription factor DEC1 is required for efficient autoreactive CD4+ T cell response. *J Exp Med* **210**:1603–1619.
Masoumi F, Ghorbani S, Talebi F, Branton WG, Rajaei S, Power C, Noorbakhsh F. 2019. Malat1 long noncoding RNA regulates inflammation and leukocyte differentiation in experimental autoimmune

encephalomyelitis. *J Neuroimmunol* **328**:50–59.
Matloubian M, Kolhekar SR, Somasundaram T, Ahmed R. 1993. Molecular determinants of macrophage tropism and viral persistence: importance of single amino acid changes in the polymerase and glycoprotein of lymphocytic choriomeningitis virus. *J Virol* **67**:7340–7349.
Mi H, Muruganujan A, Huang X, Ebert D, Mills C, Guo X, Thomas PD. 2019. Protocol Update for large-scale genome and gene function analysis with the PANTHER classification system (v.14.0). *Nat Protoc* **14**:703–721.
Milner JJ, Nguyen H, Omilusik K, Reina-Campos M, Tsai M, Toma C, Delpoux A, Boland BS, Hedrick SM, Chang JT, Goldrath AW. 2020. Delineation of a molecularly distinct terminally differentiated memory CD8 T cell population. *Proc Natl Acad Sci U S A* **117**:25667–25678.
Murali-Krishna K, Altman JD, Suresh M, Sourdive DJ, Zajac AJ, Miller JD, Slansky J, Ahmed R. 1998. Counting antigen-specific CD8 T cells: a reevaluation of bystander activation during viral infection. *Immunity* **8**:177–187.
Nakagawa S, Ip JY, Shioi G, Tripathi V, Zong X, Hirose T, Prasanth KV. 2012. Malat1 is not an essential component of nuclear speckles in mice. *RNA* **18**:1487–1499.
Olson JA, McDonald-Hyman C, Jameson SC, Hamilton SE. 2013. Effector-like CD8$^+$ T cells in the memory population mediate potent protective immunity. *Immunity* **38**:1250–1260.
Pipkin ME, Sacks JA, Cruz-Guilloty F, Lichtenheld MG, Bevan MJ, Rao A. 2010. Interleukin-2 and Inflammation Induce Distinct Transcriptional Programs that Promote the Differentiation of Effector Cytolytic T Cells. *Immunity* **32**:79–90.
Poliseno L, Salmena L, Zhang J, Carver B, Haveman WJ, Pandolfi PP. 2010. A coding-independent function of gene and pseudogene mRNAs regulates tumour biology. *Nature* **465**:1033–1038.
Ponting CP, Haerty W. 2022. Genome-Wide Analysis of Human Long Noncoding RNAs: A Provocative Review. *Annu Rev Genomics Hum Genet*. doi:10.1146/annurev-genom-112921-123710
Qiao Y, Peng C, Li J, Wu D, Wang X. n.d. LncRNA MALAT1 is Neuroprotective in a Rat Model of Spinal Cord Ischemia-Reperfusion Injury Through miR-204 Regulation. *Curr Neurovasc Res* **15**:211–219.
Quinlan AR. 2014. BEDTools: The Swiss-Army Tool for Genome Feature Analysis. *Curr Protoc Bioinformatics* **47**:11.12.1–34.
Ross CJ, Rom A, Spinrad A, Gelbard-Solodkin D, Degani N, Ulitsky I. 2021. Uncovering deeply conserved motif combinations in rapidly evolving noncoding sequences. *Genome Biol* **22**:29.
Roychoudhuri R, Clever D, Li P, Wakabayashi Y, Quinn KM, Klebanoff CA, Ji Y, Sukumar M, Eil RL, Yu Z, Spolski R, Palmer DC, Pan JH, Patel SJ, Macallan DC, Fabozzi G, Shih H-Y, Kanno Y, Muto A, Zhu J, Gattinoni L, O'Shea JJ, Okkenhaug K, Igarashi K, Leonard WJ, Restifo NP. 2016. BACH2 regulates CD8(+) T cell differentiation by controlling access of AP-1 factors to enhancers. *Nat Immunol* **17**:851–860.
Shapiro VS, Truitt KE, Imboden JB, Weiss A. 1997-7. CD28 mediates transcriptional upregulation of the interleukin-2 (IL-2) promoter through a composite element containing the CD28RE and NF-IL-2B AP-1 sites. *Mol Cell Biol* **17**:4051–4058.
Shehata HM, Khan S, Chen E, Fields PE, Flavell RA, Sanjabi S. 2018. Lack of Sprouty 1 and 2 enhances survival of effector CD8+ T cells and yields more protective memory cells. *Proc Natl Acad Sci U S A* **115**:E8939–E8947.
Su K, Wang N, Shao Q, Liu H, Zhao B, Ma S. 2021. The role of a ceRNA regulatory network based on lncRNA MALAT1 site in cancer progression. *Biomed Pharmacother* **137**:111389.
Suresh M, Whitmire JK, Harrington LE, Larsen CP, Pearson TC, Altman JD, Ahmed R. 2001. Role of CD28-B7 interactions in generation and maintenance of CD8 T cell memory. *J Immunol* **167**:5565–5573.
Toumi R, Yuzefpolskiy Y, Vegaraju A, Xiao H, Smith KA, Sarkar S, Kalia V. 2022. Autocrine and paracrine IL-2 signals collaborate to regulate distinct phases of CD8 T cell memory. *Cell Rep* **39**:110632.
Tripathi V, Ellis JD, Shen Z, Song DY, Pan Q, Watt AT, Freier SM, Bennett CF, Sharma A, Bubulya PA, Blencowe BJ, Prasanth SG, Prasanth KV. 2010. The nuclear-retained noncoding RNA MALAT1 regulates alternative splicing by modulating SR splicing factor phosphorylation. *Mol Cell* **39**:925–938.
Vandenberghe P, Verwilghen J, Van Vaeck F, Ceuppens JL. 1993. Ligation of the CD5 or CD28 molecules on resting human T cells induces expression of the early activation antigen CD69 by a calcium- and tyrosine kinase-dependent mechanism. *Immunology* **78**:210–217.
Wang Q-M, Lian G-Y, Song Y, Huang Y-F, Gong Y. 2019. LncRNA MALAT1 promotes tumorigenesis and immune escape of diffuse large B cell lymphoma by sponging miR-195. *Life Sci* **231**:116335.
Weirick T, Militello G, Müller R, John D, Dimmeler S, Uchida S. 2016. The identification and characterization of

novel transcripts from RNA-seq data. *Brief Bioinform* **17**:678–685.
Welten SPM, Redeker A, Franken KLMC, Oduro JD, Ossendorp F, Čičin-Šain L, Melief CJM, Aichele P, Arens R. 2015. The viral context instructs the redundancy of costimulatory pathways in driving CD8(+) T cell expansion. *Elife* **4**. doi:10.7554/eLife.07486
Wherry EJ, Ahmed R. 2004. Memory CD8 T-cell differentiation during viral infection. *J Virol* **78**:5535–5545.
Whyte CE, Singh K, Burton OT, Aloulou M, Kouser L, Veiga RV, Dashwood A, Okkenhaug H, Benadda S, Moudra A, Bricard O, Lienart S, Bielefeld P, Roca CP, Naranjo-Galindo FJ, Lombard-Vadnais F, Junius S, Bending D, Hochepied T, Halim TYF, Schlenner S, Lesage S, Dooley J, Liston A. 2022. Context-dependent effects of IL-2 rewire immunity into distinct cellular circuits. *J Exp Med* **219**. doi:10.1084/jem.20212391
Wigton EJ, Mikami Y, McMonigle RJ, Castellanos CA, Wade-Vallance AK, Zhou SK, Kageyama R, Litterman A, Roy S, Kitamura D, Dykhuizen EC, Allen CDC, Hu H, O'Shea JJ, Ansel KM. 2021. MicroRNA-directed pathway discovery elucidates an miR-221/222-mediated regulatory circuit in class switch recombination. *J Exp Med* **218**. doi:10.1084/jem.20201422
Wilusz JE, Sunwoo H, Spector DL. 2009. Long noncoding RNAs: functional surprises from the RNA world. *Genes Dev* **23**:1494–1504.
Wojciechowski S, Tripathi P, Bourdeau T, Acero L, Grimes HL, Katz JD, Finkelman FD, Hildeman DA. 2007. Bim/Bcl-2 balance is critical for maintaining naive and memory T cell homeostasis. *J Exp Med* **204**:1665–1675.
Wu J, Zhang H, Zheng Y, Jin X, Liu M, Li S, Zhao Q, Liu X, Wang Y, Shi M, Zhang S, Tian J, Sun Y, Zhang M, Yu B. 2018. The Long Noncoding RNA MALAT1 Induces Tolerogenic Dendritic Cells and Regulatory T Cells via miR155/Dendritic Cell-Specific Intercellular Adhesion Molecule-3 Grabbing Nonintegrin/IL10 Axis. *Front Immunol* **9**:1847.
Xiao H, Tang K, Liu P, Chen K, Hu J, Zeng J, Xiao W, Yu G, Yao W, Zhou H, Li H, Pan Y, Li A, Ye Z, Wang J, Xu H, Huang Q. 2015. LncRNA MALAT1 functions as a competing endogenous RNA to regulate ZEB2 expression by sponging miR-200s in clear cell kidney carcinoma. *Oncotarget* **6**:38005–38015.
Xie H, Liao X, Chen Z, Fang Y, He A, Zhong Y, Gao Q, Xiao H, Li J, Huang W, Liu Y. 2017. LncRNA MALAT1 Inhibits Apoptosis and Promotes Invasion by Antagonizing miR-125b in Bladder Cancer Cells. *J Cancer* **8**:3803–3811.
Yao Y, Guo W, Chen J, Guo P, Yu G, Liu J, Wang F, Liu J, You M, Zhao T, Kang Y, Ma X, Yu S. 2018. Long noncoding RNA Malat1 is not essential for T cell development and response to LCMV infection. *RNA Biol* **15**:1477–1486.
Yoon J-H, Abdelmohsen K, Srikantan S, Yang X, Martindale JL, De S, Huarte M, Zhan M, Becker KG, Gorospe M. 2012. LincRNA-p21 suppresses target mRNA translation. *Mol Cell* **47**:648–655.
Zhang B, Arun G, Mao YS, Lazar Z, Hung G, Bhattacharjee G, Xiao X, Booth CJ, Wu J, Zhang C, Spector DL. 2012. The lncRNA Malat1 Is Dispensable for Mouse Development but Its Transcription Plays a cis-Regulatory Role in the Adult. *CellReports* **2**:111–123.